Experimental study on vortex-induced motions of a semi-submersible platform with four square columns, Part I: Effects of current incidence angle and hull appendages

Rodolfo T. Gonçalves [a,*], Guilherme F. Rosetti [a], André L.C. Fujarra [a], Allan C. Oliveira [b]

[a] TPN—Numerical Offshore Tank, Department of Naval Architecture and Ocean Engineering, Escola Politécnica—University of São Paulo, Av. Professor Mello Moraes, 2231, Cidade Universitária, São Paulo, SP 05508-030, Brazil
[b] CENPES—Research and Development Center, Petrobras, Rio de Janeiro, RJ, Brazil

ARTICLE INFO

ABSTRACT

An experimental study on Vortex-Induced Motion (VIM) of the semi-submersible platform concept with four square columns is presented. Model tests were carried out to check the influence of different headings and hull appendages (riser supports located at the pontoons; fairleads and the mooring stretches located vertically at the external column faces; and hard pipes located vertically at the internal column faces). The results comprise in-line, transverse and yaw motions, as well as combined motions in the *XY* plane, drag and lift forces and spectral analysis. The main results showed that VIM in the transverse direction occurred in a range of reduced velocity 4.0 up to 14.0 with amplitude peaks around reduced velocities around 7.0 and 8.0. The largest transverse amplitudes obtained were around 40% of the column width for 30° and 45° incidences. Another important result observed was a considerable yaw motion oscillation, in which a synchronization region could be identified as a resonance phenomenon. The largest yaw motions were verified for the 0° incidence and the maxima amplitudes around 4.5°. The hull appendages located at columns had the greatest influence on the VIM response of the semi-submersible.

1. Introduction

The Vortex-Induced Motion (VIM) of semi-submersible recently emerged as an important issue in offshore and ocean engineering, mainly with the development of deep draft semi-submersibles. It is a more complex phenomenon than the VIM of cylindrical structures, such as spars and monocolumns, as a consequence of the wake interaction of vortices shed from multiple columns. In this context, the study aims at experimentally demonstrating the presence of VIM on a semi-submersible platform with four square columns and, at the same time, to verify two important design aspects, namely the heading of the platform relative to the incoming flow and the position of hull appendages. Further studies concerning the coexistence of vortex shedding and waves and the effects of different levels of damping and drafts will be reported in the second part of this publication.

Section 2 presents a background of VIM phenomenon as well as a background of vortex shedding around multi-array cylinders.

The experimental setup and details about the reduced scale model are described in Section 3. The analysis methodology of the tests is presented in Section 4. The results concerning amplitudes of motions in the transverse and in-line directions, as well as characteristic yaw motion amplitudes are discussed in Section 5. In the same section, force coefficients (drag and lift), coupled motions in the water surface plane, oscillation frequencies and spectral analysis are presented. Finally, in Section 6, some conclusions are drawn.

2. Background

2.1. VIM of offshore floating units

As a preliminary remark regarding notation, we will herein refer to VIM as the motions induced by vortex shedding occurring on large-sized offshore floating units. In a general perspective, VIM is characterized mainly by two degrees-of-freedom (DOF) motions in the free surface, i.e. in-line and transverse direction (or in terms of typically offshore nomenclature as surge and sway motions). Recent findings account for important yaw motions under some circumstances (see e.g. Waals et al., 2007).

* Corresponding author. Tel./fax: +55 11 30911727.
E-mail addresses: rodolfo_tg@tpn.usp.br (R.T. Gonçalves),
guilherme.feitosa@tpn.usp.br (G.F. Rosetti), afujarra@usp.br (A.L.C. Fujarra),
allan_carre@petrobras.com.br (A.C. Oliveira).

Nomenclature

Δ	displacement
α	angle of attack
ω	instantaneous frequency
ρ	fluid density
$\emptyset$	current incidence angle
ζ_6	damping factor for yaw motion
ζ_y	damping facto for the motions in the transverse direction
A	characteristic yaw motion amplitude
A_0	submerged projected area for 0° incidence
A_P	submerged projected area
A_x/L	nondimensional characteristic motion amplitude in the in-line direction
A_y/L	nondimensional characteristic motion amplitude in the transverse direction
C	structural damping coefficient
C_D	drag force coefficient
C_L	lift force coefficient
C_X	force coefficient in the in-line direction
C_{XY}	moment coefficient for yaw motion
C_Y	force coefficient in the transverse direction
D	characteristic dimension of the section of the body subjected to a vortex shedding
f_{0y}	natural frequency of the motion in the transverse direction in still water
f_6	natural frequency of yaw motion in still water
F_{Hx}	hydrodynamic force acting on the system in the in-line direction
F_{Hy}	hydrodynamic force acting on the system in the transverse direction
H	immersed column height above the pontoon
$H(\omega,t)$	Hilbert spectrum
J	inertia moment for yaw motion
J_a	added inertia moment for yaw motion
L	width of the column
L_Z	vertical moment arm
m	platform mass
m_a	added mass
P	pontoon height
R	half length of the platform
Re	Reynolds number
S	distance between center columns
St	Strouhal number
T_0	natural period of the motion in the transverse direction in still water
T_6	natural period of the yaw motion in still water
U	incident current velocity
V_r	reduced velocity
V_{r6}	corrected reduced velocity for yaw motion
X	axis motion in the in-line direction
Y	axis motion in the transverse direction

The study of VIM has become of utmost importance since offshore platforms were placed in the Gulf of Mexico, USA, where the strong loop currents triggered vigorous motions due to vortex shedding. In this region, spar platforms were a good solution to explore and to produce hydrocarbons at deep water levels. However, the cylindrical shape of this type of platform with high level of current speeds is susceptible to synchronized vortex shedding that induces high motion of the order of its diameter dimension. Additionally, the large displacements and drift on the surface reflect on the design of the mooring lines and risers system regarding both extreme tension and fatigue life (see for example, Huang et al., 2003).

Experimental VIM study of spar platforms started, for example, in van Dijk et al. (2003) and Finn et al. (2003), in which the purpose was to verify the influence of the hull geometry and appendages. In turn, strake developments were conducted to mitigate the VIM phenomenon, such as in works by Irani and Finn (2005), Roddier et al. (2009) and Wang et al. (2009, 2010). These works showed that strakes can be a good solution but need to be correctly designed and tested for each particular hull. The influence of the Reynolds number was discussed in several works, mainly in Mercier and Ward (2003) and Roddier et al. (2009) and showed to be an important issue in the model test design, because tests in high Reynolds numbers minimize the boundary layer distortion, decreasing the difference between small-scale modeled Reynolds numbers and full scale ones. Roddier et al. (2009) showed that tests carried out in low Reynolds numbers presented higher amplitudes level than high Reynolds number, which implies conservative values in the design phase. On the other hand, the use of Computational Fluid Dynamics (CFD) showed to be a reasonable alternative in terms of qualitative results. Examples of CFD applications to improve the strakes performance on spar platforms can be found in Oakley Jr. and Constantinides (2007) and Wang et al. (2010) and on semi-submersibles as in Kim et al. (2011).

The VIM of monocolumn platforms showed to be important even considering their lower aspect ratio (ratio between immersed length and diameter). The characteristic aspect ratio of monocolumn and spar platforms is between one half and two diameters, respectively. Works by Cueva et al. (2006) and Gonçalves et al. (2010, 2012c) observed transverse motion amplitudes around one diameter and significant coupled motion between in-line and transverse motions, characterized by eight-shape trajectories. Numerical studies showed that the low frequency motion and high amplitude motions due to VIM are capable of damaging risers and mooring lines in monocolumn platforms, as presented in Sagrilo et al. (2009), decreasing the fatigue life by ca. 30%.

There are a number of other aspects that are relevant for VIM of both spar and monocolumn platforms, such as the concomitant presence of surface waves and the current; draft conditions or aspect ratio of the floating unit and lines-induced damping. All these aspects influence VIM and an overview about them can be found in Gonçalves et al. (2012b). Another important issue that makes the floating offshore units susceptible to the VIM phenomenon is the small mass ratio (ratio between the displaced mass and the platform mass, approximately equal to one in the case of spar and monocolumn platforms and less than one for TLP platforms, (see Waals et al. (2007)).

The confirmed presence of VIM on semi-submersibles, as reported in Rijken and Leverette (2009) from field measurements, contributes to the development of a new generation of semi-submersibles, as pointed out in Hussain et al. (2009), Xu (2011) and Noce and Husem (2011). Looking into these researches, it is possible to determine the main geometric nondimensional parameters that can affect the VIM, such as H/L, S/L and H/P; where H is the immersed column height above the pontoon, L is the width of the column, S is the distance between center columns and P is the pontoon height. These dimensions can be illustrated as in Fig. 1.

The study on VIM of semi-submersible platforms is more recent than that of cylindrical ones (spar or monocolumns). This fact arises from the increasing dimensions of the new semi-submersible platforms and from the increase of the water depth,

which can promote notable VIM. Naturally, the increasing number of squared columns semi-submersibles is the main motivation for the present work and the reason why we focus on such a particular geometric arrangement. Table 1 provides distances between columns for this type of design, from which one notes that our case falls into the typical range ($3.20 < S/L < 4.19$). Thus, we present and discuss the results for this type of design, which is representative of an important group of semi-submersibles under design and operation nowadays, especially in Brazilian waters.

In this scenario, experimental works focused on VIM of semi-submersible platforms were presented by Rijken et al. (2004, 2011), Waals et al. (2007), Rijken and Leverette (2008), Hong et al. (2008), Stansberg (2008), Magee et al. (2011) and Tahar and Finn (2011). All of these works reported relevant motions in certain current conditions, which can reduce the fatigue life of steel catenary risers (SCR) by as much as 50% near the touch-down point (TDP), as noted in Xiang et al. (2010) and Cheng et al. (2011).

Another point not thoroughly discussed in VIM studies of cylindrical platforms but one that has shown to be important for semi-submersibles platforms is the yaw motion. Waals et al. (2007) was the pioneer to report significant yaw amplitudes.
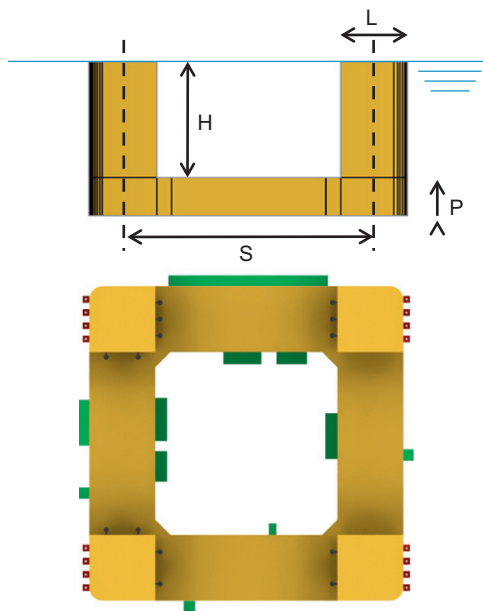

Fig. 1. Characteristic dimensions of a four-column semi-submersible.

Hussain et al. (2009) and Magee et al. (2011) endorsed that this is a relevant issue.

The works outlined previously were the references and support to our experimental work. Table 1 also presents a summary of the VIM results for semi-submersibles, according to which comparisons were made to emphasize and to confirm the results.

2.2. Vortex shedding on multi-array cylinders

The geometry of the semi-submersible platforms implies a more complex VIM phenomenon than that identified for single cylindrical structures. In the case of semi-submersible platforms, the vortex shedding occurs from each column and thus the wake interference, different for each current incidence (platform heading), characterizes the VIM of the unit.

The semi-submersible studied herein presents four square columns, which increase the differences as compared with circular cylinders. As mentioned, the importance of this geometry is justified upon the existence of several similar operating floating units in which VIM has been reported (see Rijken and Leverette, 2009). Thus, our study is motivated by a practical demand.

For square sections, the incidence angle is important owing to the non-axial symmetry. Norberg (1993) experimentally investigated the flow and pressure forces on fixed rectangular cylinders at angles of incidence from 0° up to 90°. The Strouhal numbers obtained for square cylinders for 0° incidence (flow perpendicular to the square face) and for 45° incidence were, respectively, $St = 0.13$ and 0.17. The drag force coefficients, C_D, reached the maximum value of $C_D = 2.2$ for 0° incidence, value approximately two times as high as the one from circular cylinders. The works by Dutta et al. (2003, 2008) and Yen and Yang (2011) showed the flow patterns and vortex shedding behavior behind a fixed square cylinder through visualization techniques, confirming the results by Norberg (1993).

The flow interference between four equally spaced cylinders is significant to understand the behavior of semi-submersible platforms subject to current incidence. The effects of interference between circular cylinders in different array configurations were discussed by Zdravkovich (1987) and later between four equally spaced cylinders by Sayers (1988, 1990). These works evaluated force coefficients for fixed arrays of different ratios between the center-to-center cylinder spacing S and their diameter D, S/D, and different current incidence angles. Lam and Lo (1992) and Lam and Fang (1995) carried out similar tests comparing to those by Sayers, employing the dye injection visualization method to determine the flow pattern. Recently, Lam performed measurements using particle image visualization (PIV), completing his

Table 1
Summary of the main works published about VIM of semi-submersible platforms. One should notice that the characteristic amplitudes are defined differently in each paper. Here all these results were put on the same basis.

	H/L	S/L	H/P	Re	Vr	Max. A/L45 at 45°
Rijken et al. (2004)	2.18	3.75	4.83	1×10^4–1×10^5	1.0–11.0	0.85
Waals et al. (2007)	1.75/0.87	4.14	2.33/1.16	6×10^3–7×10^4	4.0–40.0	0.65/0.14
Stansberg (2008)	nd	4.08	nd	nd	nd	nd
Rijken and Leverette (2008)	2.18	3.75	4.83	$\sim 10^5$	1.0–15.0	0.85
Hong et al. (2008)	nd	4.19		4×10^4–2×10^5	9.6 & 17.4	0.22
Hussain et al. (2009)	nd	nd	nd	nd	5.0–21.0	0.85
Rijken et al. (2011)	1.71	4.04	3.04	3×10^4—3×10^5	5.0–9.0	0.64
Cheng et al. (2011)	nd	nd	nd	nd	nd	nd
Magee et al. (2011)	1.50/1.00	nd	nd	nd	4.0–14.0	0.50/0.15
Xu (2011)	1.55/1.15	3.65	3.10/1.92	nd	4.0–15.0/3.0–15.0	0.56/0.28
Tahar and Finn (2011)	1.74	3.20	4.00	Up to 5×10^5	2.0–15.0	0.51
Present work	1.14	3.76	1.98	6×10^3–9×10^4	2.5–20.0	0.40
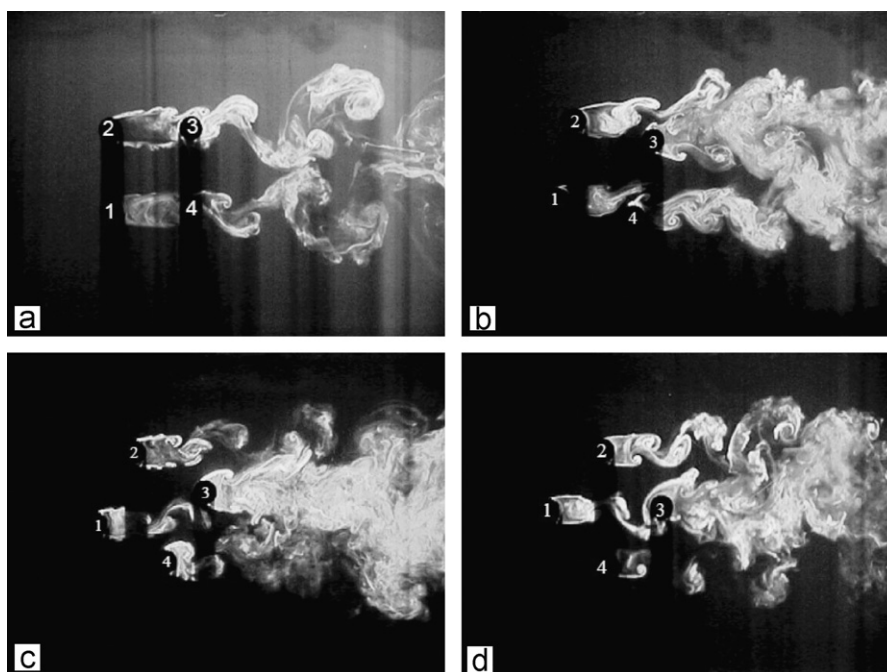
Fig. 2. Typical flow pattern for different current incidence angles: (a) ∅=0°, (b) ∅=15°, (c) ∅=30° and (d) ∅=45° and S/D=4.00 in water tunnel. *Source*: Lam et al. (2003b).

research. In Lam et al. (2003a, 2003b), results were published about Strouhal number and force coefficients (drag and lift). The results were presented for each cylinder separately and for the complete array of cylinders.

The main findings of the works with arrays of cylinders were that, for a range of spacing ratio between $1.70 < S/L < 4.00$ (in our case, S/L=3.76) the upstream cylinders experienced larger mean drag force than the downstream ones, while the downstream cylinders are usually subjected to higher fluctuating forces under the influence of unsteady wake vortices for all incidence angles. Also in this range, distinct vortex shedding of the upstream cylinders was suppressed; see examples in Fig. 2.

When spacing ratio values decrease below S/L=1.70, only a wide wake is found attached to the doublet of cylinders, similar to the behavior of a single cylinder. For values of spacing ratio above S/L=4.00, the wake is well established in each of the four cylinders. These statements may account for excitation forces in the VIM phenomenon of semi-submersible platforms, in which the value of spacing ratios are around S/L=4.00 (see Table 1). To the authors' knowledge, no works about fundamental issues of flow induced vibration on four cylinders array free to oscillate were found in the open literature in order to be compared with VIM studies of semi-submersibles. The present work intends to make this link.

3. Experimental setup

The experimental setup is characterized by a small-scale model of the semi-submersible unit supported by a set of equivalent moorings in the towing tank at the Institute of Technological Research (IPT) in São Paulo, Brazil.

The setup is towed by the main car together with the instrumentation for monitoring the important physical parameters of the VIM phenomenon, in this case: motions in 6 degrees-of-freedom; including in-line and transverse motions; forces in each of the four springs that compose the equivalent mooring system and the towing velocity.

Table 2
Main characteristics of the semi-submersible unit. The adopted scale was 1:100 and it was tested in two different draft conditions. In this work, only the operational full draft of 34 m was presented.

Distance between center columns (S)	74.52 m
Immersed column height above the pontoon (H)	22.60 m
Width of the column (L)	19.80 m
Pontoon height (P)	11.40 m
Displacement (Δ)	105,237 tons

3.1. Small-scale model

The definition of the reduced scale was made based on the dimensions of the test basin at the IPT ($4.0 \times 6.6 \times 280.0$ m, respectively, depth × width × length). The possible velocities that may be developed by the main car of the towing tank were also a determinant factor for that definition. These two factors were important to define the magnitude of the typical periods of oscillation due to VIM and, therefore, to determine the number of oscillation cycles acquired. At least 30 cycles in steady state were acquired, representing a useful length of 180 m in the towing tank at the maximum velocity of 0.30 m/s. A minimum of 30 cycles in steady state is necessary to characterize the VIM phenomenon and to guarantee good statistics. The time limit of tests was 15 min.

The main dimensions of the semi-submersible are presented in Table 2, based on the dimensions defined in Fig. 1.

According to Fig. 3, only the relevant hydrodynamic appendages were represented, such as: the riser supports located at the pontoons; the fairleads and the mooring stretches vertically at the external column faces; and the hard pipes located vertically at the internal column faces (see details in Figs. 4–6).

As extremely high Reynolds numbers are involved in field conditions, the usual procedure for reliable VIM tests of floating units is based on the Froude scaling, resulting in the relation

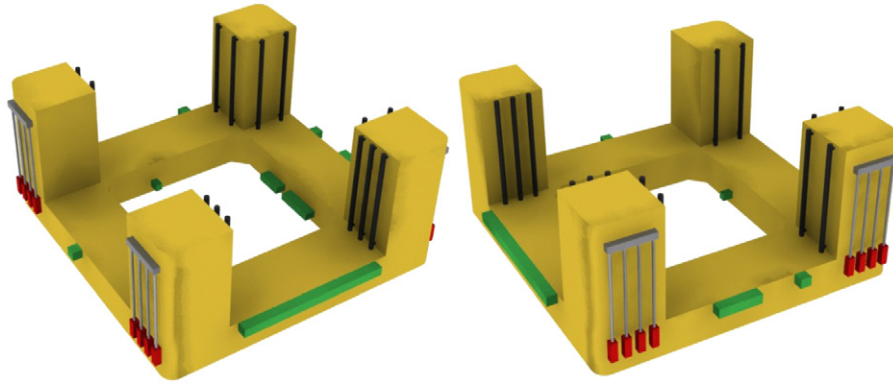$$Re_{model} = Re_{full}\lambda^{3/2} \tag{1}$$

Fig. 3. Artistic 3D view of semi-submersible model with the hydrodynamic appendages modeled.
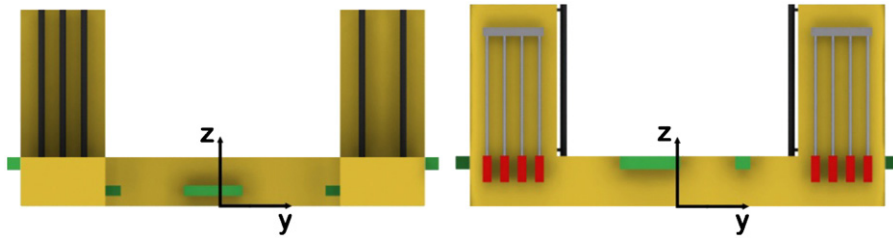

Fig. 4. Front view of the semi-submersible model showing the position of fairleads, mooring lines and hard pipes, in red, gray and black, respectively, at columns. (For interpretation of the references to color in this figure legend, the reader is referred to the web version of this article.)
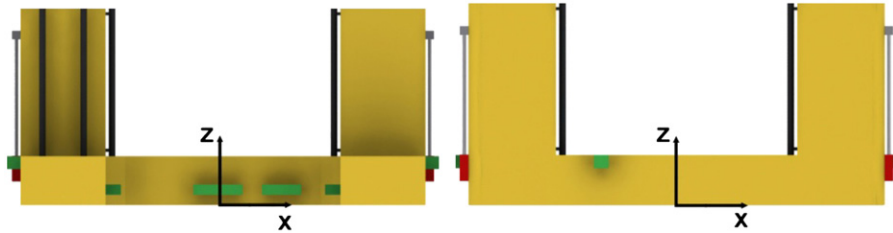

Fig. 5. Lateral view of the semi-submersible model showing the riser supports position, in green at pontoons. (For interpretation of the references to color in this figure legend, the reader is referred to the web version of this article.)

Fig. 6. Picture of the semi-submersible model scaled in 1:100.

where Re_{model} and Re_{full} are the Reynolds number in the model scale condition and full (field) scale one, respectively; and λ is the scale factor.

By hypothesis, the corners of the square columns of semi-submersible are as separation points, thus assumed to be enough to guarantee that the scale effects are less relevant than in cylinders (see Fujarra et al., 2012).

Fig. 6 presents details of the semi-submersible small-scale model. The model was built in fiber glass and surface roughness was not included. As commented in Rijken and Leverette (2008), the roughness is not so important in the case of four square columns, as the vortex generation typically occurs along the down-current column faces at the column corners. The correct gravity center was adjusted by ballasts inside pontoons and columns. A wood deck above the water line was constructed to support the measurement system (targets for an optical motion capture device) and ballast to fine adjust inertial properties.

3.2. Equivalent mooring

The model was built with a ring located in the column portions above the water level to fix the equivalent mooring system, as can be seen in Figs. 7 and 8. That ring allowed the same mooring configuration for all the different current incidences, i.e. the same value of mooring stiffness, important to compare the results for all the different current incidences tested. The mooring stiffness was scaled to be similar to the full scale condition (1:1) in 45° heading. The values of mooring stiffness performed were 13.91 and 21.49 N/m to in-line and transverse direction, respectively. Therefore, the natural periods in the water surface plane was the
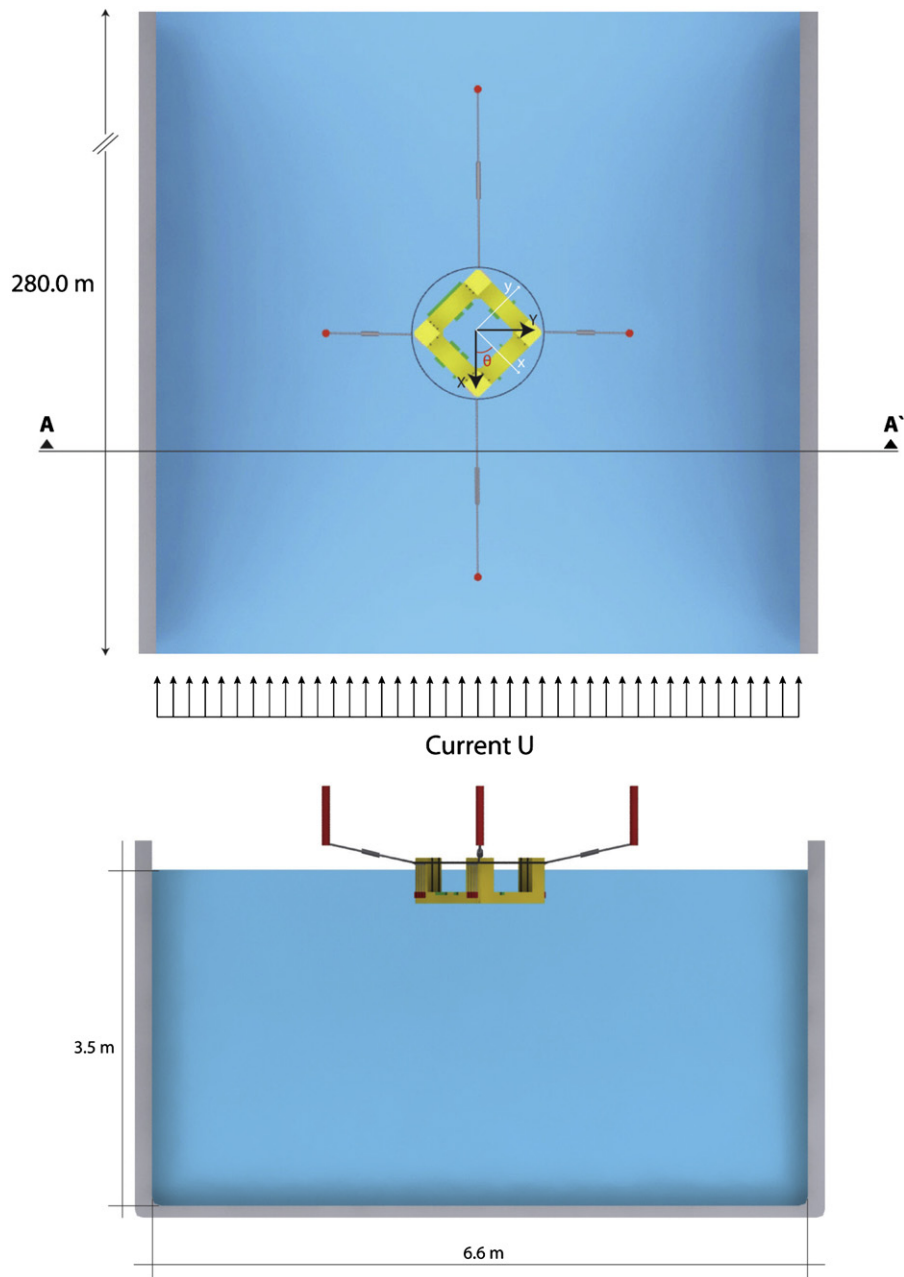
Fig. 7. Sketch of the equivalent mooring system stupe composed of four lines at the IPT towing tank.

same for the different heading conditions as presented in Table 3. The mooring lines were designed to avoid disturbing the vortex shedding, as can be seen in detail in Figs. 8 and 9.

3.3. The test program

Fig. 9 shows the coordinate system in 2D horizontal plane. The X and Y axes represent the (basin-fixed) global coordinate system, and x and y are the (body-fixed) local coordinate system. In all the tests, current flow comes from $+X$ and $-X$. The incident current angle, $\emptyset$, is defined as the counterclockwise angle from the vector current U (along X) to the axis x.

The current incidences tested were: 0°, 15°, 30°, 45°, 180°, 195°, 210° and 225°. The angles were defined according to Fig. 9. At least 18 different reduced velocities were tested for each condition. The range of current velocities conducted were 0.03 up to 0.30 m/s, which corresponds to a Reynolds number range of 6000 up to

85,000 and a reduced velocity range of $2.5 \leq V_r \leq 20.0$. The Froude number tested was lower than 0.2, which indicates that the viscous effects are more important than the gravitational ones.

4. Analysis methodology

4.1. Motion amplitudes

The experimental results of the VIM on the small-scale model of the semi-submersible platform were analyzed by means of the Hilbert–Huang Transform method (HHT), as presented in Gonçalves et al. (2012a). The procedure is summarized as follows.

The HHT was developed by Huang et al. (1998) as an alternative to deal with non-stationary signals that arise from non-linear systems. This analysis applies the typical Hilbert transform to a finite set of 'Intrinsic Mode Functions' (IMFs), which are

obtained from the original signal through an 'Empirical Mode Decomposition' (EMD). The EMD method is based on a recursive subtraction of successively calculated means between the two time-envelope of extrema contained in the signal (maxima and minima), which are then spline fitted. Such a recursive procedure is carried out for each IMF limited by a standard deviation stopping condition that is applied at each step. The IMF set is complete by construction.

Considering $Z_j(t)$ as an analytic function, for example, one of the IMFs is defined as follows:

$$Z_j(t) = X_j(t) + iY_j(t) = a_j(t)exp[i\theta_j(t)] \qquad (2)$$

The real part, $X_j(t)$ is the proper IMF and the complex part is the Hilbert Transform of $X_j(t)$, with P standing for the principal value.

$$Y_j(t) = \frac{1}{\pi}P\int_{-\infty}^{+\infty}\frac{X_j(\tau)}{t-\tau}\,d\tau \qquad (3)$$

Accordingly, the original signal can be decomposed into the IMF set, as in a 'generalized Fourier series':

$$X(t) = Re\sum_{j=1}^{n}a_j(t)exp\left[i\int\omega_j(t)dt\right] \qquad (4)$$

$$\omega_j(t) = \frac{d}{dt}[\theta_j(t)] \qquad (5)$$

where not only the amplitude $a_j(t)$ but also the local phase $\theta_j(t)$ and thus the local (or instantaneous) frequency $\omega_j(t)$ of each IMF are time dependent, this one formalized through the stationary phase method, as pointed out in Huang et al. (1998).

By performing this analysis, the amplitude and the instantaneous frequency can be presented as functions of time in a three-dimensional plot; the so-called Hilbert spectrum, $H(\omega,t)$.

Consequently, the HHT is extremely indicated for amplitude and frequency modulation, characteristics frequently found in VIM signals. The distribution of energy is more accurately performed as energy can be locally concentrated in a specific range of frequencies.

As VIM signals can be non-stationary, it is also difficult to define the amplitude of the signal by usual Fast Fourier Transform (FFT) analysis. This is another issue that HHT can resolve as local amplitude is obtained regardless of the non-stationary behavior.

A time history of a typical VIM signal in the transverse direction has few peaks in the signal (for example, 30 peaks including maxima and minima) which may give rise to poor statistic characteristics for the evaluation of the characteristic amplitude in the transverse direction as a mean of the 20% highest peaks, i.e. mean of only 6 points.

The nondimensional amplitude was defined by taking the mean of the 10% largest amplitudes as obtained in the HHT, both for motion in the transverse and in-line directions, and the yaw motion. In the HHT, the amplitude is time function, and then the mean of the 10% largest amplitudes is proportional to the length of data and the sampling frequency.

4.2. Reduced velocity

The reduced velocity is defined as

$$V_r = (UT_0)/D \qquad (6)$$

where U is the incident current velocity, T_0 is the natural period of motion in the transverse direction in still water and D is the characteristic length of the section of the body subjected to a vortex shedding. In the case of VIM of semi-submersible, the value D can be written as a function of the current incidence angle, in order to better represent the characteristic length of the
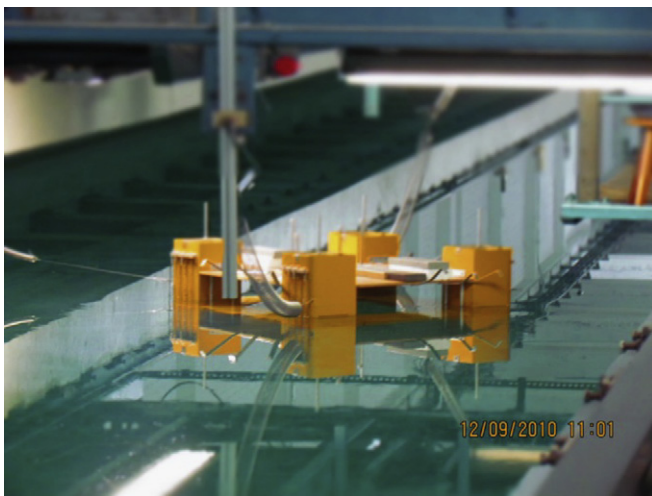

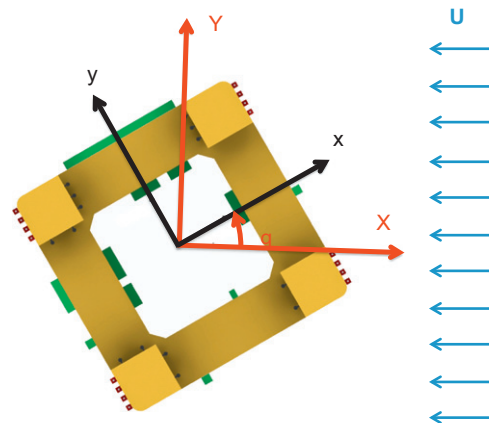Fig. 8. Picture of a run test at 45° incidence at the IPT towing tank.

Fig. 9. Top view of the semi-submersible model showing the definition of incidence angles and hull appendages position.

Table 3
Natural periods in the water surface in still waters. Values in model scale.

Incidence angle, $\emptyset$	Natural period in the in-line direction or surge motion, T_{0X} (s)	Natural period in the transverse direction or sway motion, T_{0Y} or T_0 (s)	Natural period of yaw motion, T_6 (s)
0° and 180°	22.45	18.57	9.40
15° and 195°	22.63	18.82	9.43
30° and 210°	22.34	18.22	9.40
45° and 225°	22.89	18.42	9.35

column section on the flow, i.e.

$$D = L(|\sin\emptyset| + |\cos\emptyset|) \tag{7}$$

where L is the width of the column and $\emptyset$ is the incident current angle. Details of the nomenclature and definitions can be seen in Fig. 10.

The motion characteristic amplitudes in the transverse and in-line direction are non-dimensioned by the width of the column L, i.e. it is the same value for all incidence conditions. This choice permits to directly compare results from different incidence conditions.

4.3. Hydrodynamic forces

The linear rigid body motion equations for a platform with two uncoupled degree-of-freedom, in-line and transverse direction, are represented by the following equations proposed and discussed in Sarpkaya (2004) as shown below:

$$m\ddot{X}(t) + C\dot{X}(t) + K_x X(t) = F_{Hx}(t) \tag{8}$$

$$m\ddot{Y}(t) + C\dot{Y}(t) + K_y Y(t) = F_{Hy}(t) \tag{9}$$

where m represents the platforms mass; C the structural damping coefficient of the system; F_{Hy} and F_{Hx} are the total hydrodynamic forces acting on the system in the in-line, X, and transverse, Y, directions. In these equations, the 'structural' forces are placed on the left side of the equations; and the hydrodynamic forces, which include added mass (in phase with acceleration) and hydrodynamic damping (in phase with velocity) and other forces due to fluid, are placed on the right side of the equations.

In the experiments, the total hydrodynamic forces in each given direction are measured indirectly using these motion equations. The total hydrodynamic force is the sum of the inertial, dissipative, and restoring forces of the system (the restoring forces were derived from the measurement using four load cells, one in each mooring spring; then the force is decomposed in the in-line and transverse direction, also considering the yaw angle of the platform). Preliminarily, the structural dissipative force (structural damping) can be disregarded, considering it has a smaller magnitude value than the other forces involved in the system dynamics. Therefore, the hydrodynamic force is obtained by the sum of the restoring and inertial forces.

The force in the transverse direction to the flow, or transverse direction, Y, is commonly represented in the form of the non-dimensional lift coefficient, C_L, as in

$$F_{Hy}(t) = \tfrac{1}{2}\rho A_P U^2 C_L(t) \tag{10}$$

$$C_L(t) = \frac{2F_{Hy}(t)}{\rho A_P U^2} \tag{11}$$

where ρ is the fluid density, A_P is the submerged projected area of the platform in relation to the transverse direction to the flow. The non-time dependent lift coefficient, C_L, is evaluated as a mean of the 20% highest peaks as well as the characteristic motion amplitudes using HHT.

The force in the in-line direction, X, can be divided into two parts, one related to the average drag force (static component) and a second one related to the dynamic drag force (oscillatory component). Thus, the average part of the drag can be described as

$$\overline{F_{Hx}(t)} = \tfrac{1}{2}\rho A_P U^2 C_D \tag{12}$$

$$C_D = \frac{2\overline{F_{Hx}(t)}}{\rho A_P U^2} \tag{13}$$

where $\overline{F_{Hx}(t)}$ is the average total hydrodynamic force in the in-line direction and C_D is the average drag coefficient.

The submerged projected area for a single circular cylinder is not dependent on the current incidence angle, but for an array of square cylinders this is different. Fig. 11 shows the perspective for the different incidence angles of the semi-submersible studied, and Table 4 presents the respective values of the submerged projected area. The force coefficient results will be presented using the area for 0° incidence and also using the values for each incidence angle.
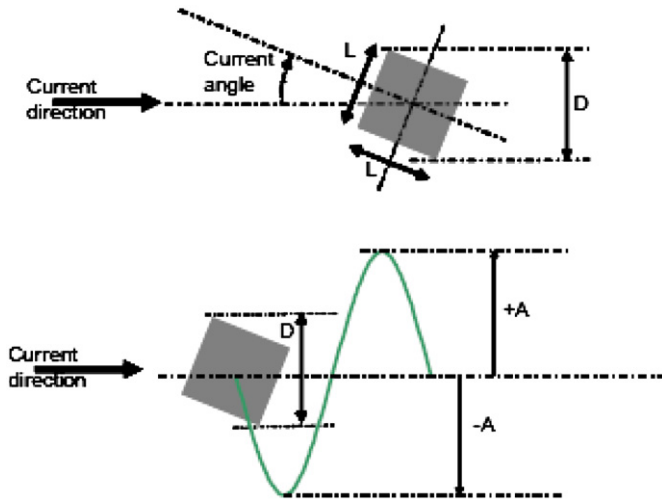

Fig. 10. Definition of parameters A (characteristic amplitude), D (projected length) and L (column dimension).
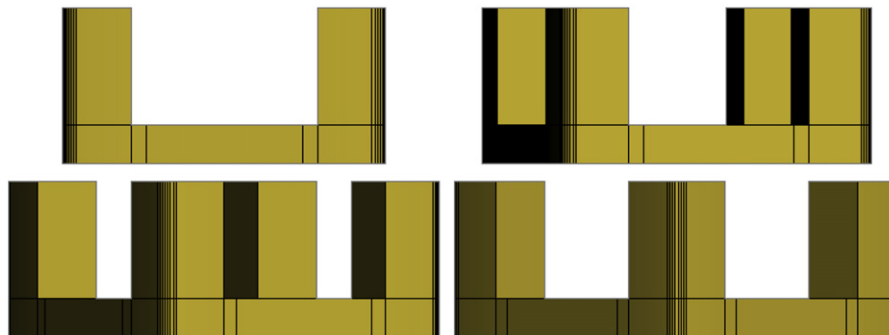*Source*: Rijken and Leverette (2008).

Fig. 11. Submerged projected area for a semi-submersible platform for different incidence angles: (a) $\emptyset = 0°$, (b) $\emptyset = 15°$, (c) $\emptyset = 30°$ and (d) $\emptyset = 45°$.

Table 4
Submerged projected area for a semi-submersible for different incidence angles. Values for real scale.

Incidence angle, ∅	Submerged projected area for a semi-submersible, A_P (m²)
0° and 180°	1967.15
15° and 195°	3220.61
30° and 210°	3814.47
45° and 225°	3301.88
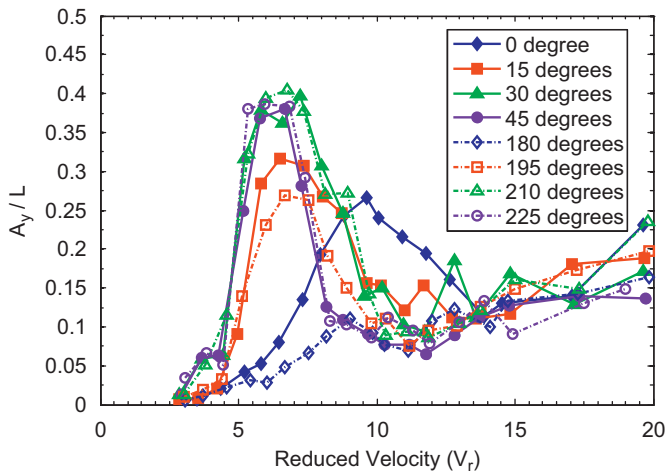
Fig. 12. Nondimensional amplitudes for the motions in the transverse direction for different current incidences: 0°, 15°, 30°, 45°, 180°, 195°, 210° and 225°.

5. Experimental results

In this section, some of the most important results of the analysis of the phenomenon on VIM of semi-submersible will be presented.

5.1. Motions in the transverse direction

Fig. 12 presents the results of nondimensional characteristic amplitude for motion in the transverse direction for 0°, 15°, 30°, 45°, 180°, 195°, 210°, 225° incidences. According to those results, the 30°, 45°, 210° and 225° showed the largest VIM amplitudes in the transverse direction. The values obtained were around $A_y/L \cong 0.4$ for $7.0 \leq V_r \leq 8.0$. Additionally, the largest amplitude values for 15° and 195° incidence occur at the same range of $7.0 \leq V_r \leq 8.0$ but with a reduced value of $A_y/L \cong 0.3$. Except for the 0° and 180° incidences, all the other incidences showed a range of synchronization at reduced velocity greater than 4.0 and less than about 14.0. The synchronization range for 0° and 180° is different from other ones owing to the different Strouhal number for these configurations. This fact confirms the results by Norberg (1993), in which the Strouhal number is lower for 0° incidence for a fixed square cylinder. The motion results in the transverse direction corroborate the existence of a resonant behavior on VIM of a semi-submersible platform for a range of reduced velocities, similar to the VIV phenomenon.

It is important to highlight that for $V_r > 14.0$, it is not possible to define one oscillation frequency. In this region, there is no synchronization between the vortex shedding and the natural period of the motion in the transverse direction, and then there is no pronounced VIM. The possibility of a galloping phenomenon for high reduced velocities was mentioned by Waals et al. (2007), but this behavior was not confirmed until $V_r=20$ herein; additionally, the phase

diagram of velocity versus displacement did not show characteristics of a galloping phenomenon for higher reduced velocities; the displacement is not in phase with the velocity, unlike a galloping behavior characteristic.

According to Fig. 12, the asymmetry caused by the appendages is more pronounced for 0° and 180° incidences. This difference may be attributed to the presence and position of the hard pipes on the columns for 180° incidence (see details in Fig. 9), which promotes a great modification in the wakes and, consequently, a loss in the shedding synchronization, implying reduced motions in the transverse direction. For 0° incidence, the hard pipes are immersed in the wakes, which do not influence the vortex shedding, implying motions in the transverse direction larger than those for the 180° incidence. The same asymmetry promoted by the presence of hard pipes can also be illustrated by comparing the 15° and 195° incidences. The other current incidences 30° and 210°, and 45° and 225°, did not show any influence due to the asymmetry of the appendages.

Similar conclusions are presented by Rijken et al. (2011). Rijken showed a significant influence caused by the hull appendages located on the columns and a small influence caused by the ones located on the pontoons. In addition, the effect of the hull
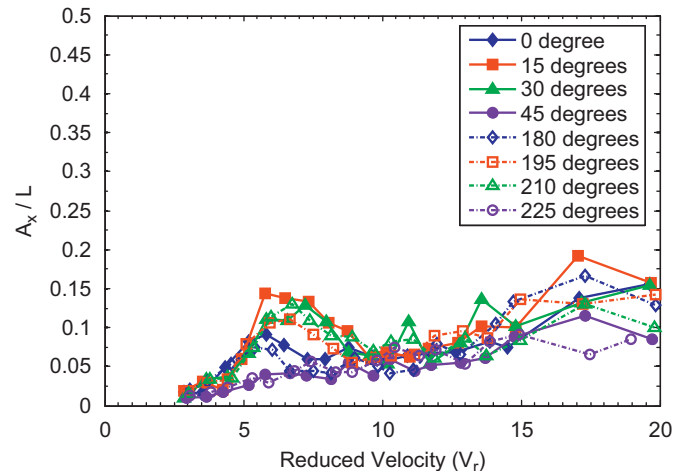
Fig. 13. Nondimensional amplitudes for the motions in the in-line direction for different current incidences: 0°, 15°, 30°, 45°, 180°, 195°, 210° and 225°.
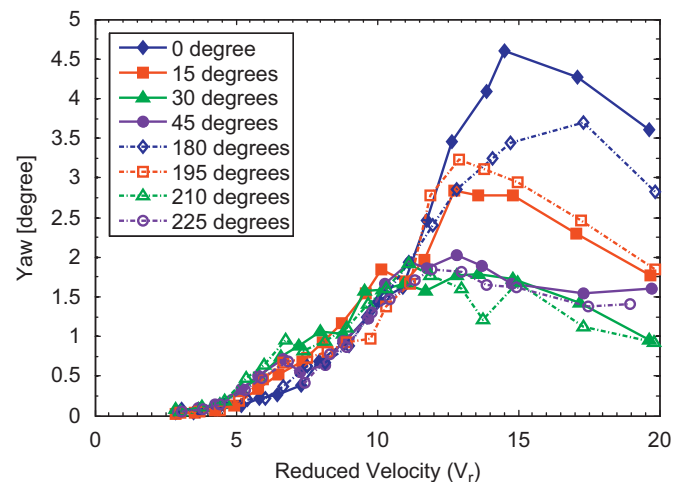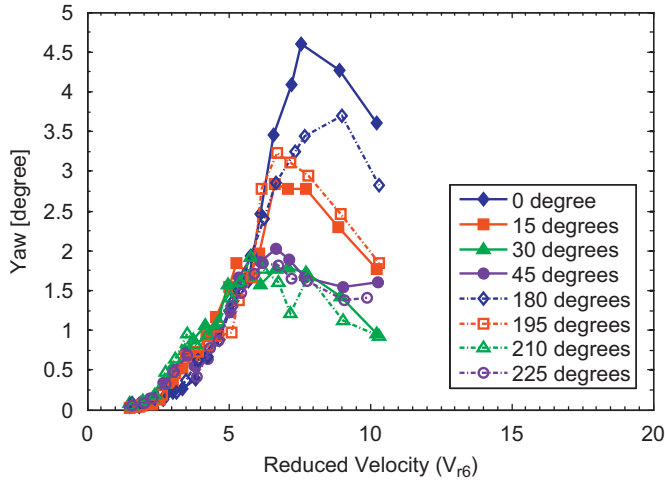

Fig. 14. Yaw characteristic amplitudes for different current incidences: 0°, 15°, 30°, 45°, 180°, 195°, 210° and 225°.
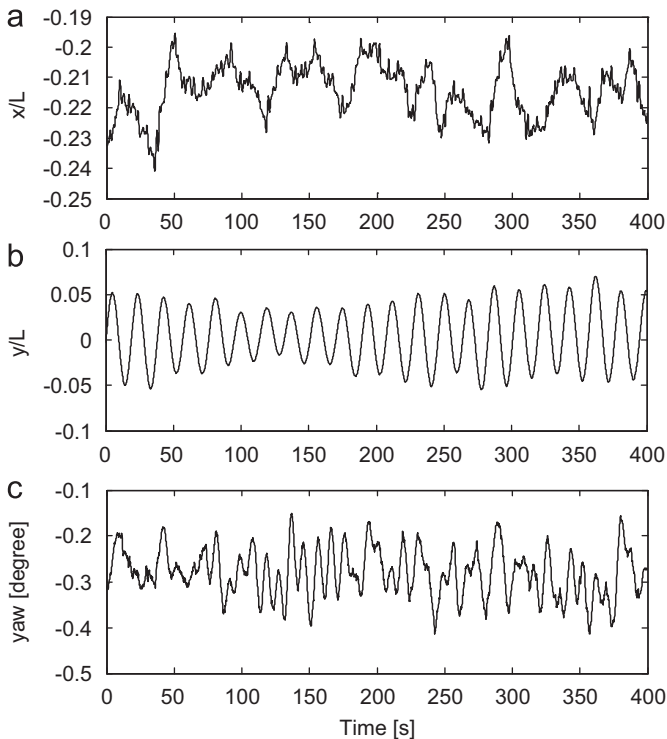
details appears to have only a small effect on the response for 45° incidence.

5.2. Motions in the in-line direction

Fig. 13 presents the results of nondimensional characteristic amplitudes for the motion in the in-line direction for 0° up to 225° incidences. According to these results, the 15°, 30°, 195° and 210° incidences showed the largest VIM amplitudes in the in-line direction. The values obtained were around $A_x/L \cong 0.15$ for $6.0 \leq V_r \leq 8.0$. The motions in the in-line direction showed to be non-periodic for $V_r \geq 10.0$; as a consequence, the values of A_x/L are

very difficult to determine. A little difference in the in-line motion due to the asymmetry of the hull appendages cannot be verified, except for the 45° and 225° incidence.

Fig. 15. Yaw characteristic amplitudes for different current incidences: 0°, 15°, 30°, 45°, 180°, 195°, 210° and 225°; as a function of corrected reduced velocity ($V_{r6} = UT_6/D$), where T_6 is the natural period of the yaw motion in still waters.
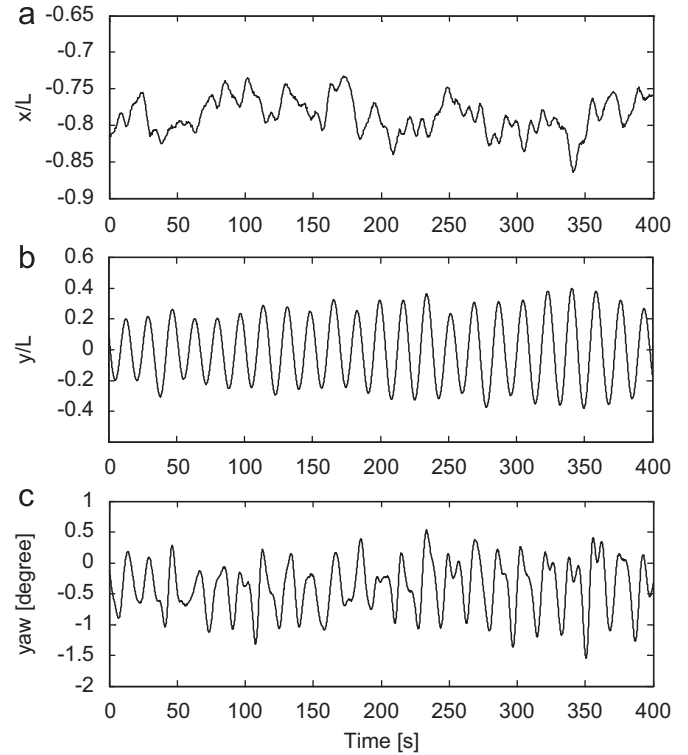
Fig. 17. Example of time history for $V_r = 6.76$ and 45° incidence for the motions: (a) in-line direction, (b) transverse direction, and (c) yaw.

Fig. 16. Example of time history for $V_r = 3.78$ and 45° incidence for the motions: (a) in-line direction, (b) transverse direction, and (c) yaw.
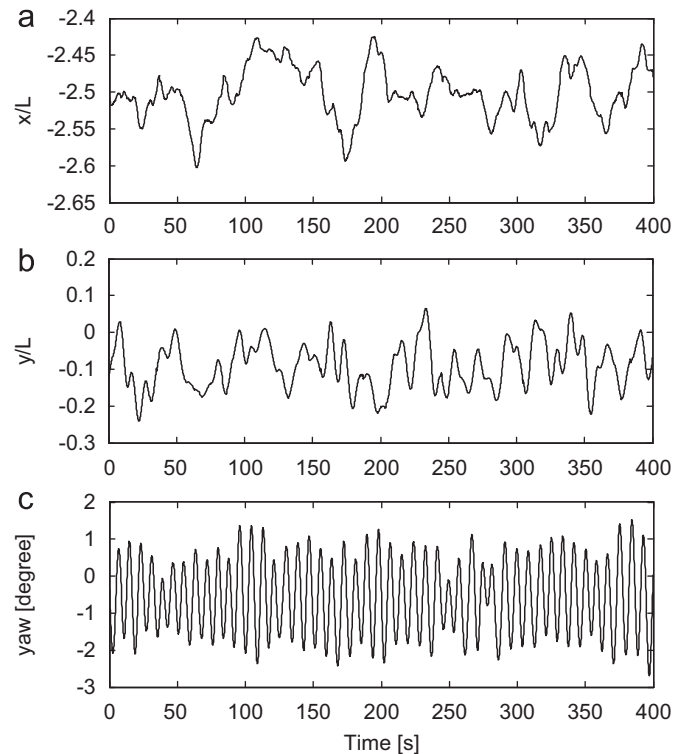
Fig. 18. Example of time history for $V_r = 12.06$ and 45° incidence for the motions: (a) in-line direction, (b) transverse direction, and (c) yaw.

5.3. Yaw motions

Fig. 14 presents the results of yaw characteristic amplitudes for 0°, 15°, 30°, 45°, 180°, 195°, 210° and 225° incidences.

According to this figure, a high amplitude behavior of the yaw can be identified. Waals et al. (2007) also identified considerable values of yaw motions in their experiments with some type of semi-submersible platforms, concluding that the yaw was
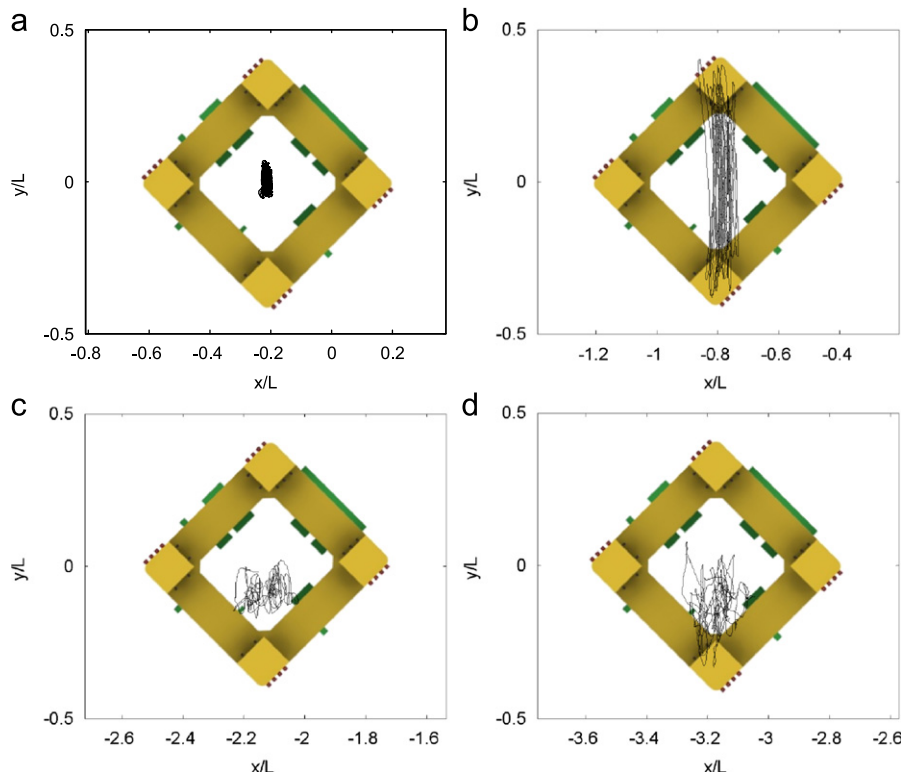

Fig. 19. Example of the motions in the XY plane for 45° incidence for different reduced velocity: (a) V_r=3.68; (b) V_r=6.68; (c) V_r=11.78; and (d) V_r=14.77.
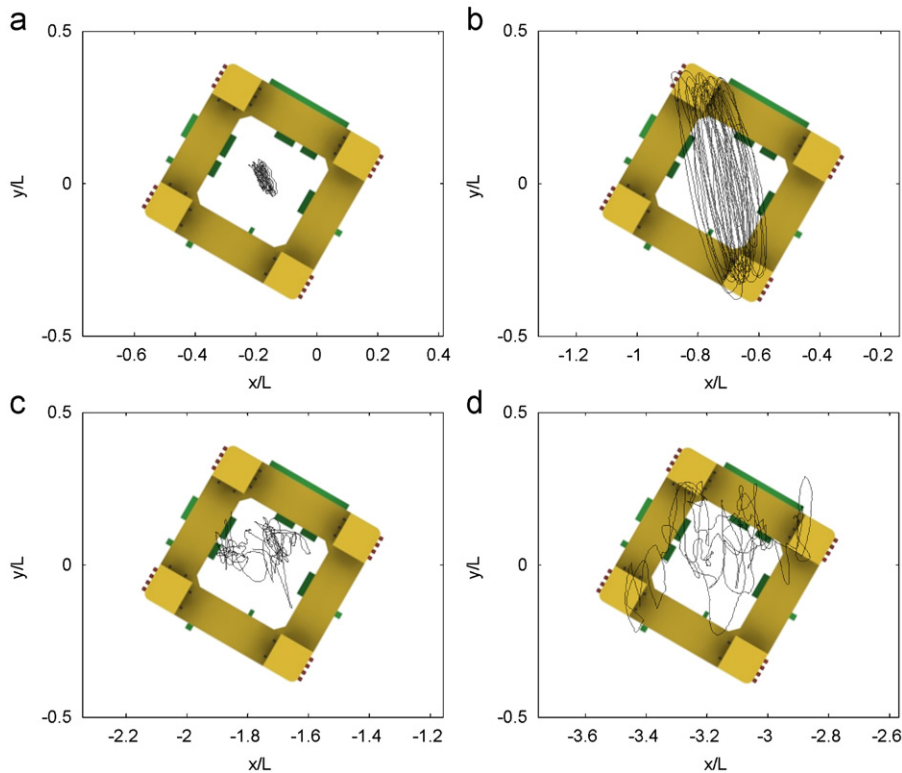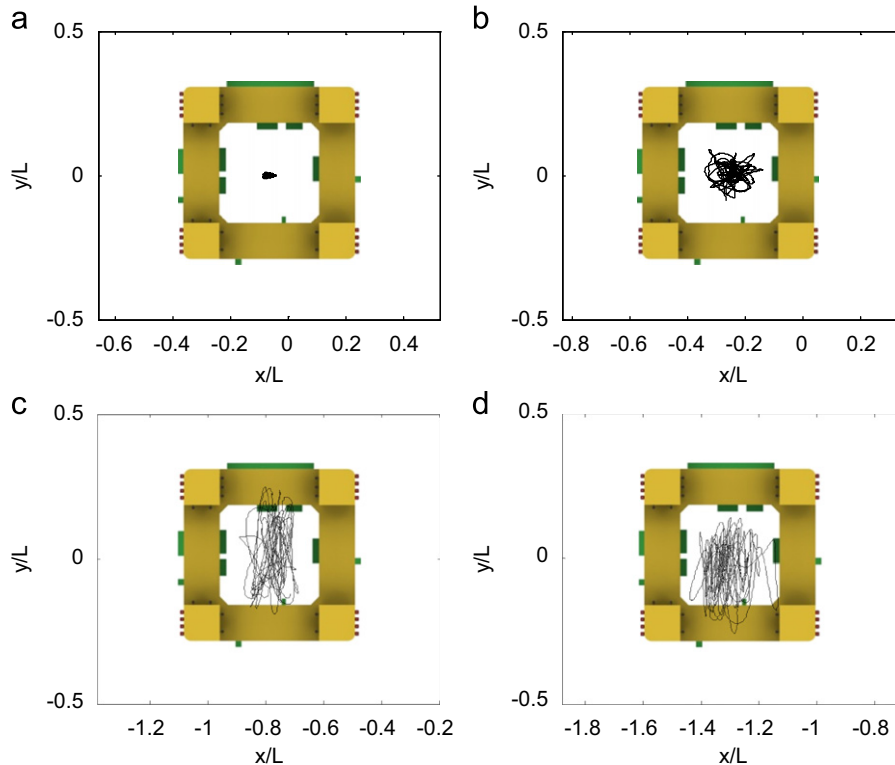

Fig. 20. Example of the motions in the XY plane for 30° incidence for different reduced velocity: (a) V_r=3.65; (b) V_r=6.60; (c)V_r=11.73; and (d) V_r=14.82.

observed as a consequence of a galloping phenomenon. According to the classical theory, the presence of a galloping phenomenon cannot be confirmed for reduced velocities up to 20, as those herein presented.

The results presented herein suggest the existence of a synchronization regime in yaw. This phenomenon occurs when the vortex shedding frequency, deriving from columns interference, gets similar to the natural frequency of yaw motion of the semi-submersible.
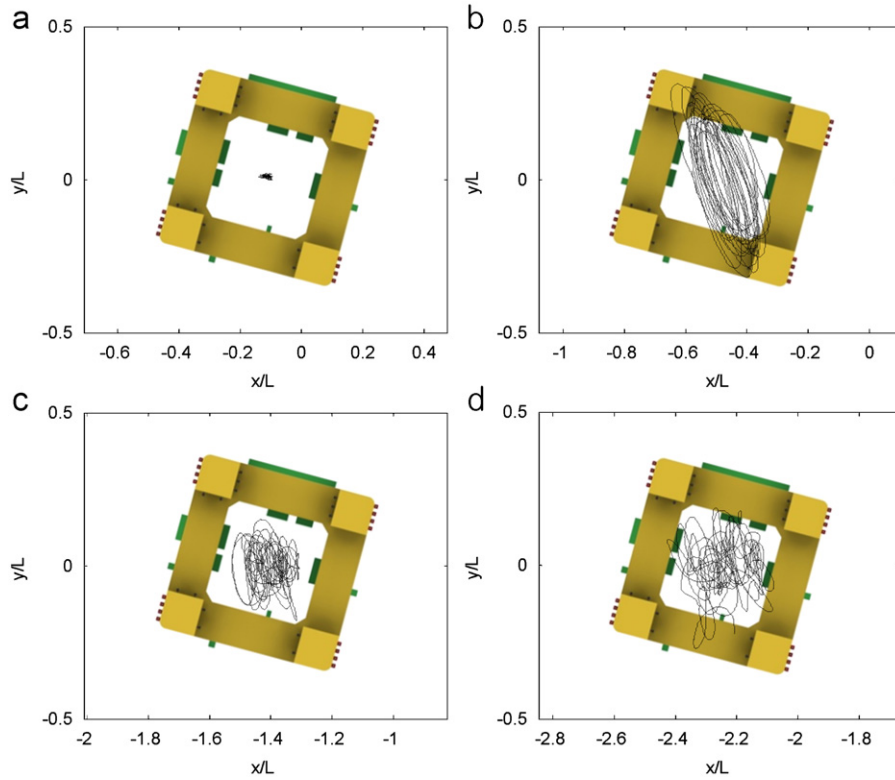
Fig. 21. Example of the motions in the *XY* plane for 15° incidence for different reduced velocity: (a) $V_r=3.55$; (b) $V_r=6.50$; (c) $V_r=11.69$; and (d) $V_r=14.82$.

Fig. 22. Example of the motions in the *XY* plane for 0° incidence for different reduced velocity: (a) $V_r=3.51$; (b) $V_r=6.47$; (c) $V_r=11.77$; and (d) $V_r=14.53$.

The synchronization for the yaw motions (see Fig. 14), are presented for a range of $14.0 \le V_r \le 16.0$ differently for motions in the transverse direction in which the synchronization range is $5.0 \le V_r \le 10.0$. This fact is due to the larger natural frequency for yaw motions than the transverse ones, which implies larger current velocity to evidence the synchronization for yaw motions. About the influences of the hull appendages in the yaw motion, it is possible to verify the largest yaw amplitudes $A \cong 4.5°$ for $0°$ and $180°$ incidences. Only in those current incidences is it possible to verify the influence of the asymmetry of the hull appendages.

The reduced velocities for yaw motions were re-calculated using the yaw natural period in still waters, T_6, to suggest a typical behavior of VIM for this degree-of-freedom. The new graphic is presented in Fig. 15. According to this figure, the largest yaw amplitudes occur for $V_r \cong 8.0$, a very similar result to that usually observed for VIM in the transverse direction.

Moment results were not presented. However, we can conjecture that the different values of drag and lift forces for each cylinder are responsible for the fluctuating moment that will promote yaw motions in the semi-submersible, similar to the results presented in Lam et al. (2003a, 2003b), where the drag and lift coefficients for each cylinder are presented separately for an array of four equally spaced cylinders.

5.4. Time history and motions in the XY plane

Results in the XY plane and example of time history are presented in this section in order to better understand the VIM of the semi-submersible.

Fig. 16 presents the time history for $45°$ incidence for $V_r = 3.8$. This reduced velocity corresponds to a region before the synchronization in the transverse direction. In this condition, the transverse motion has a dominant oscillation frequency.

Fig. 17 presents the time history for $45°$ incidence for $V_r = 6.8$. This reduced velocity corresponds to the peak of oscillation in the synchronization region for the transverse motion. The motions in the transverse direction present a well defined oscillation frequency and large amplitudes, $A_y/L \cong 0.4$. The yaw motion, even at small oscillation amplitudes, begins to present oscillations with a frequency similar to the transverse ones. Complementarily, Fig. 18 presents the time history for $45°$ incidence for $V_r = 12.1$. This reduced velocity corresponds to the peak of yaw motions, i.e. in the yaw synchronization region. It is interesting to note that at this reduced velocity, the transverse and in-line motions do not present a characteristic periodicity but the frequency of the yaw motions is clearly defined.

Finally, the motions in the XY plane are plotted in Figs. 19–22, for $0°$, $15°$, $30°$ and $45°$ incidences for four different reduced velocities. According to these results, there are no eight-shaped trajectories as those typically presented in spar and monocolumn VIM. It is interesting to notice that the VIM response occurs primarily along the semi-submersible diagonals, except in the $0°$ incidence and it is more pronounced around the synchronization region, i.e. $V_r \cong 7.0$. This behavior was noted in Rijken and Leverette (2008) and Rijken et al. (2011). It is not possible to identify synchronization between motions in the in-line and transverse directions for $V_r > 14.0$, as discussed previously.

5.5. Drag and lift force coefficients

Figs. 23 and 24 present drag force coefficient for the different current incidence angles. The results in Fig. 23 were calculated using the same value of the submerged projected area, A_P, for $0°$ incidence, while the results in Fig. 24 were calculated using the value for each incidence angle (see Fig. 11 and Table 4 for details).

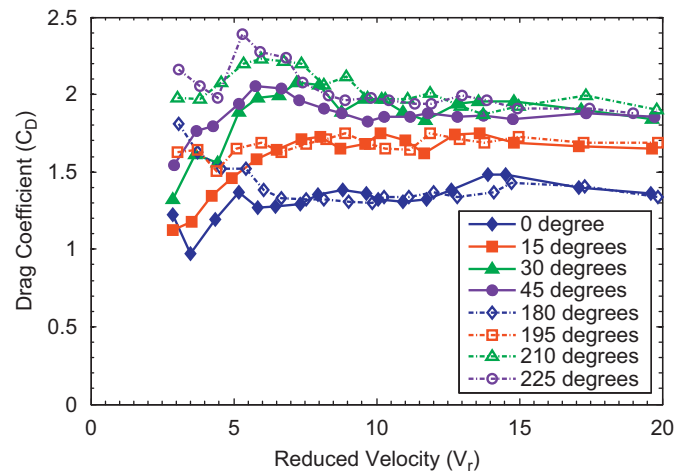**Fig. 23.** Drag force coefficient for different current incidences: $0°$, $15°$, $30°$, $45°$, $180°$, $195°$, $210°$ and $225°$. The coefficient was obtained using the submerged projected area, A_0, for $0°$ incidence.

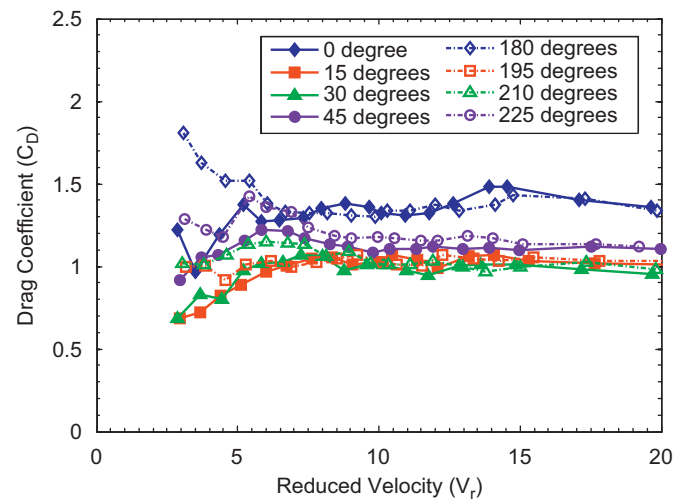**Fig. 24.** Drag force coefficient for different current incidences: $0°$, $15°$, $30°$, $45°$, $180°$, $195°$, $210°$ and $225°$. The coefficient was obtained using the corresponding submerged projected area, A_P, for each degree incidence.

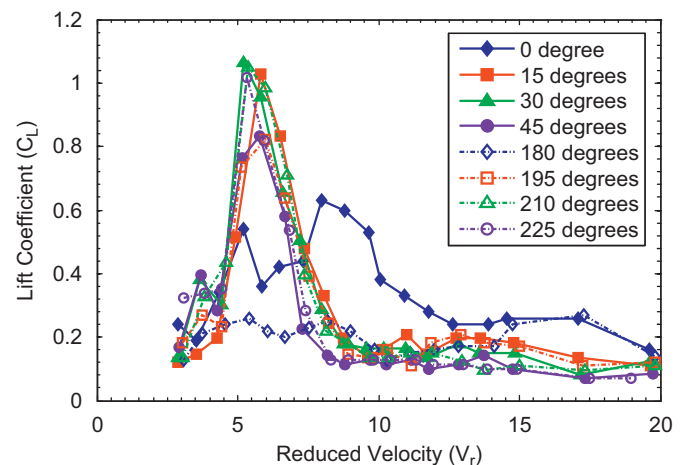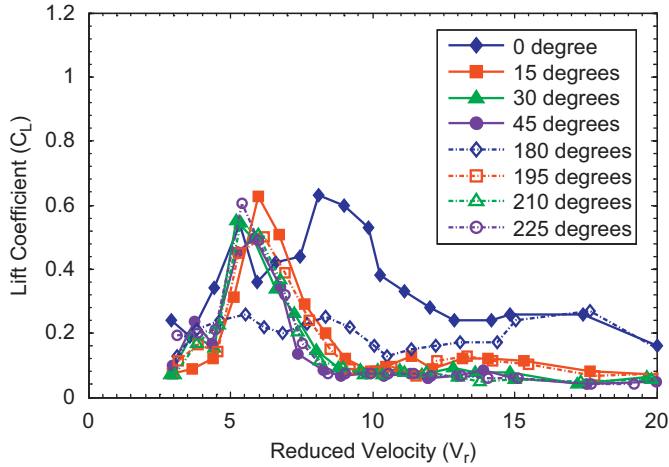**Fig. 25.** Lift force coefficient for different current incidences: $0°$, $15°$, $30°$, $45°$, $180°$, $195°$, $210°$ and $225°$. The coefficient was obtained using the submerged projected area, A_0, for $0°$ incidence.

The drag coefficient force results, in Fig. 24, present a mean trend around $C_D \approx 1.1$ for $V_r > 8.00$ except for 0° incidence, the values of which are larger, $C_D \approx 1.4$. These values are in accordance with the


Fig. 26. Lift force coefficient for different current incidences: 0°, 15°, 30°, 45°, 180°, 195°, 210° and 225°. The coefficient was obtained using the corresponding submerged projected area, A_P, for each degree incidence.

results published for an array of four equispaced cylinders, in which the 0° configuration has larger drag force (see for example Lam et al., 2003b), and they are similar to the results by Tahar and Finn (2011) for a semi-submersible. It is worth noting the dynamic drag amplification in the range $5.0 < V_r < 8.0$ for 30°, 45°, 210° and 245° incidences. The dynamic drag amplification is due to the synchronization range present in the resonance phenomenon that provides larger motion in the transverse direction. This behavior was discussed in other VIM semi-submersible tests such as Rijken et al. (2004), Rijken and Leverette (2008) and Tahar and Finn (2011).

In the same way, Figs. 25 and 26 present the lift force coefficient for the different current incidence angles. The lift coefficient force results, in Fig. 26, present a maximum value around $C_L \approx 0.7$ for all incidence angles; however, the maximum occurs for $V_r \cong 8.0$ for 0° and 180° incidences and it occurs for $V_r \cong 6.00$ for the other cases. This behavior is due to the difference in the synchronization region for each incidence angles. In all the cases, for $V_r > 10.0$, the lift coefficient values can be neglected, since no more VIM occurs in the transverse direction.

5.6. Power spectrums from FFT and HHT

Power spectrum densities (PSD) are presented in Figs. 27–29 by the FFT analysis. They are evaluated for in-line, transverse and yaw motions. The 3D graph is plotted as energy versus reduced
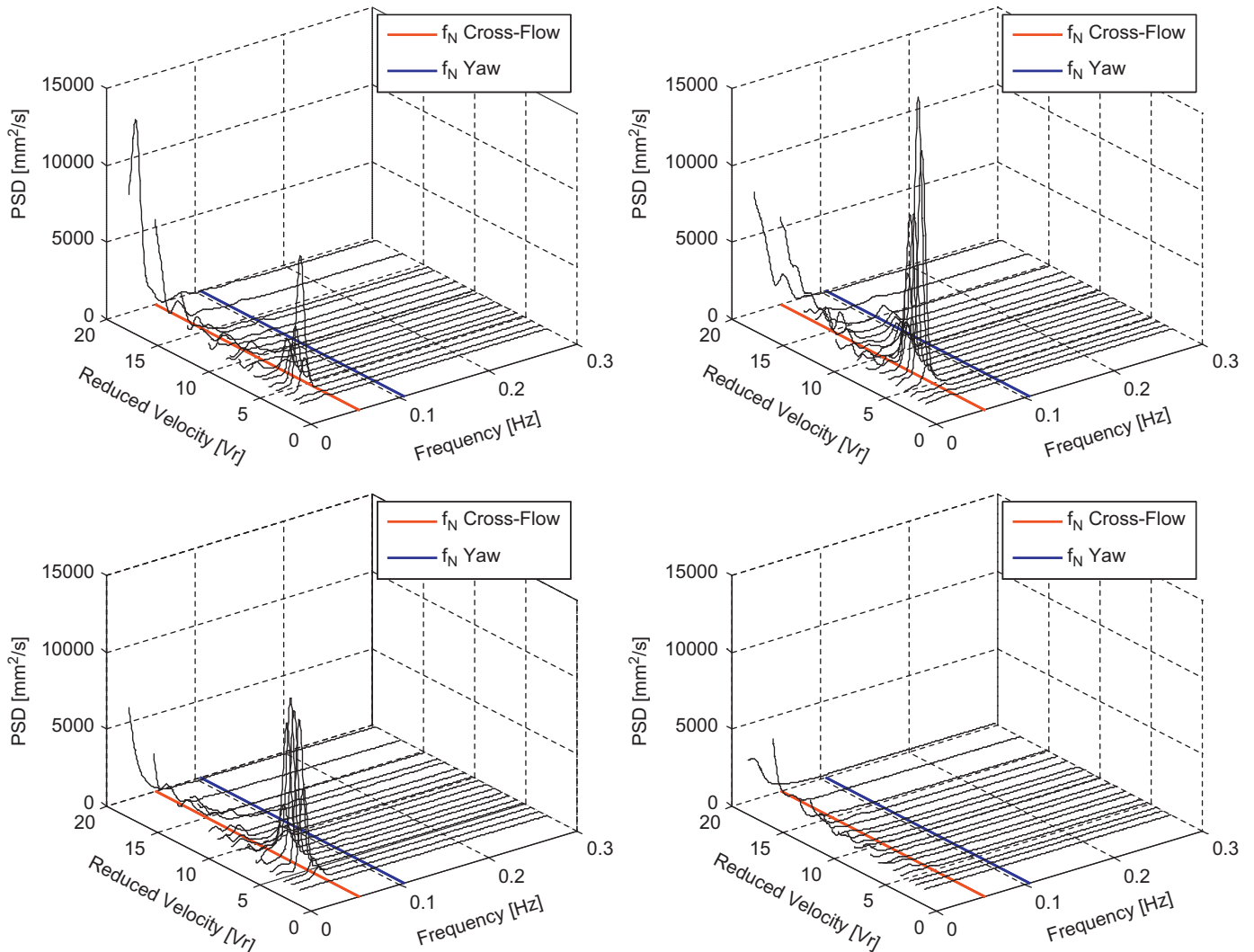
Fig. 27. Power spectrum density from FFT of the motion in the in-line direction as a function of reduced velocity and frequency for 0°, 15°, 30° and 45° incidences.
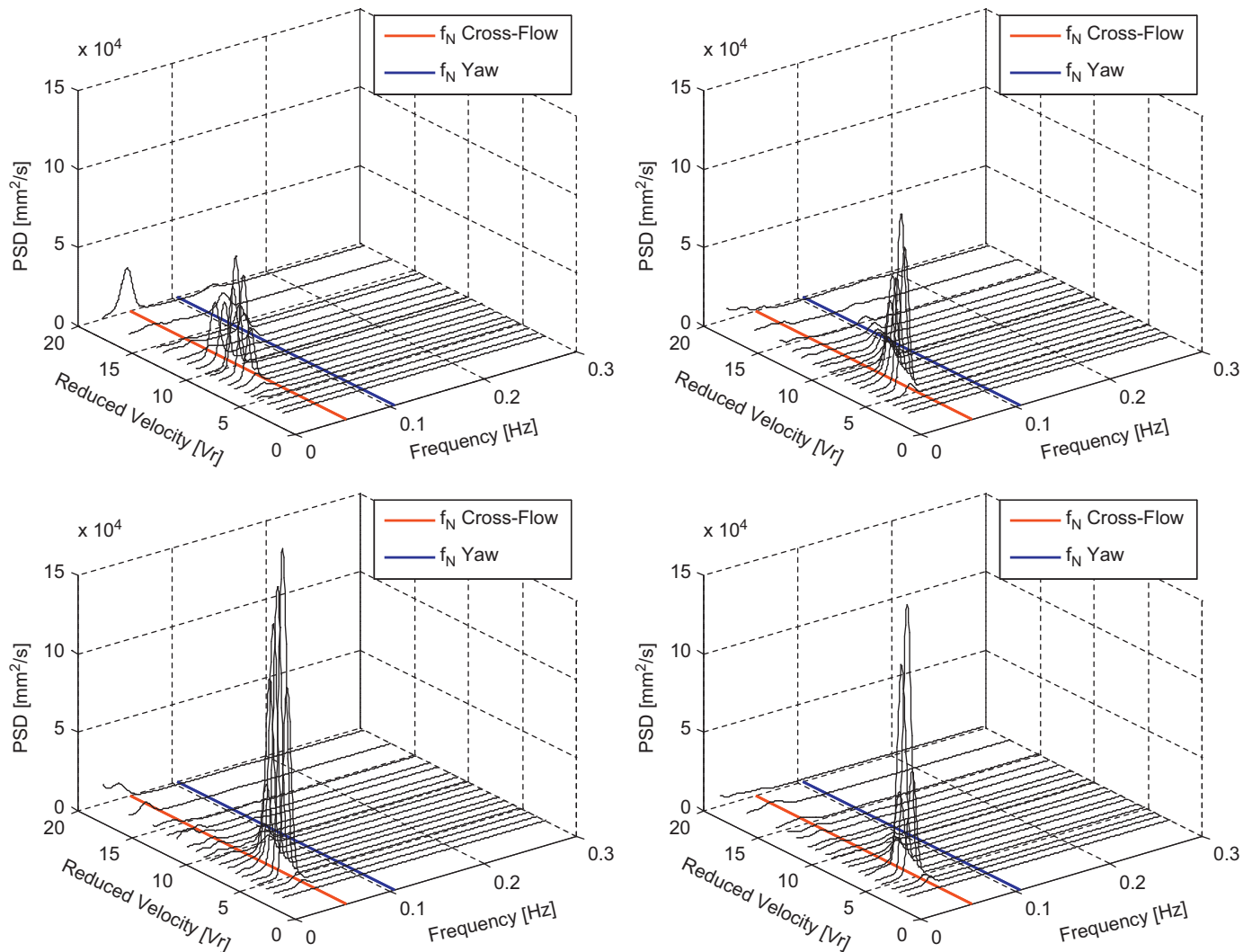
Fig. 28. Power spectrum density from FFT of the motion in the transverse direction as a function of reduced velocity and frequency for 0°, 15°, 30° and 45° incidences.

velocity versus frequency. The line representing the natural frequency of transverse motion and yaw motion are detached in all of these figures.

Fig. 27 presents the PSD for motion in the in-line direction for 0°, 15°, 30° and 45° incidences. It is possible to note the existence of appreciable energy level around the transverse natural frequency, mainly in 15° and 30° incidences. Figs. 19–22 corroborate this result, since the primary motion occurs along the semi-submersible diagonals.

The synchronization region for the motions in the transverse direction can be seen in Fig. 28. A reasonable energy level appears between reduced velocities, from 5 up to 8 for 15°, 30° and 45° incidences, and from 8 up to 11 for 0° incidence; this fact confirms the resonance behavior for the motions in the transverse direction in this range of reduced velocities; another evidence that corroborates this fact is the dominant frequency around the natural frequency of the transverse motion.

In Waals et al. (2007), similar plots were presented to confirm the existence of a high level of yaw motion in semi-submersibles subject to current incidence as in Fig. 29. In the same way as in transverse motion, it is possible to observe a resonance behavior of yaw motions, i.e. high energy level around the natural frequency of yaw motion. However, the range of synchronization occurs for higher reduced velocities $10.0 < V_r < 15.0$ due to the higher value of natural frequency of yaw than the transverse one.

Differently from motions in the transverse direction, the higher levels of energy are verified for 0° incidence, owing to higher moment caused by the wake interference in the columns for this incidence angle (see Lam et al., 2003b).

Figs. 30–32 present the Hilbert Spectrum for increasing reduced velocities, $V_r = 3.7$, 6.7 and 11.8, respectvely. The first one (Fig. 30), shows only low amplitudes for motions in the transverse direction; secondly, in Fig. 31, in the transverse synchronization range, it is possible to observe a high amplitude level of motion in the transverse direction, the motion frequency lock-in with the transverse natural frequency, and there are no considerable syncronized yaw motions; finally, in Fig. 32, the level of transverse amplitude decreases and a single frequency can no longer be defined. In this reduced velocity, $V_r = 11.8$, yaw synchronization is observed, in which high amplitude level of yaw motion around one defined frequency (natural frequency of yaw). These results support the existence of vortex-induced yaw motions (VIY) as stated before.

5.7. Complementary aspects regarding the transverse and yaw motions

As commented in Blevins (2001), a structure with noncircular cross section experiences a fluid force that changes with the orientation to the flow. As the structure moves, its orientation
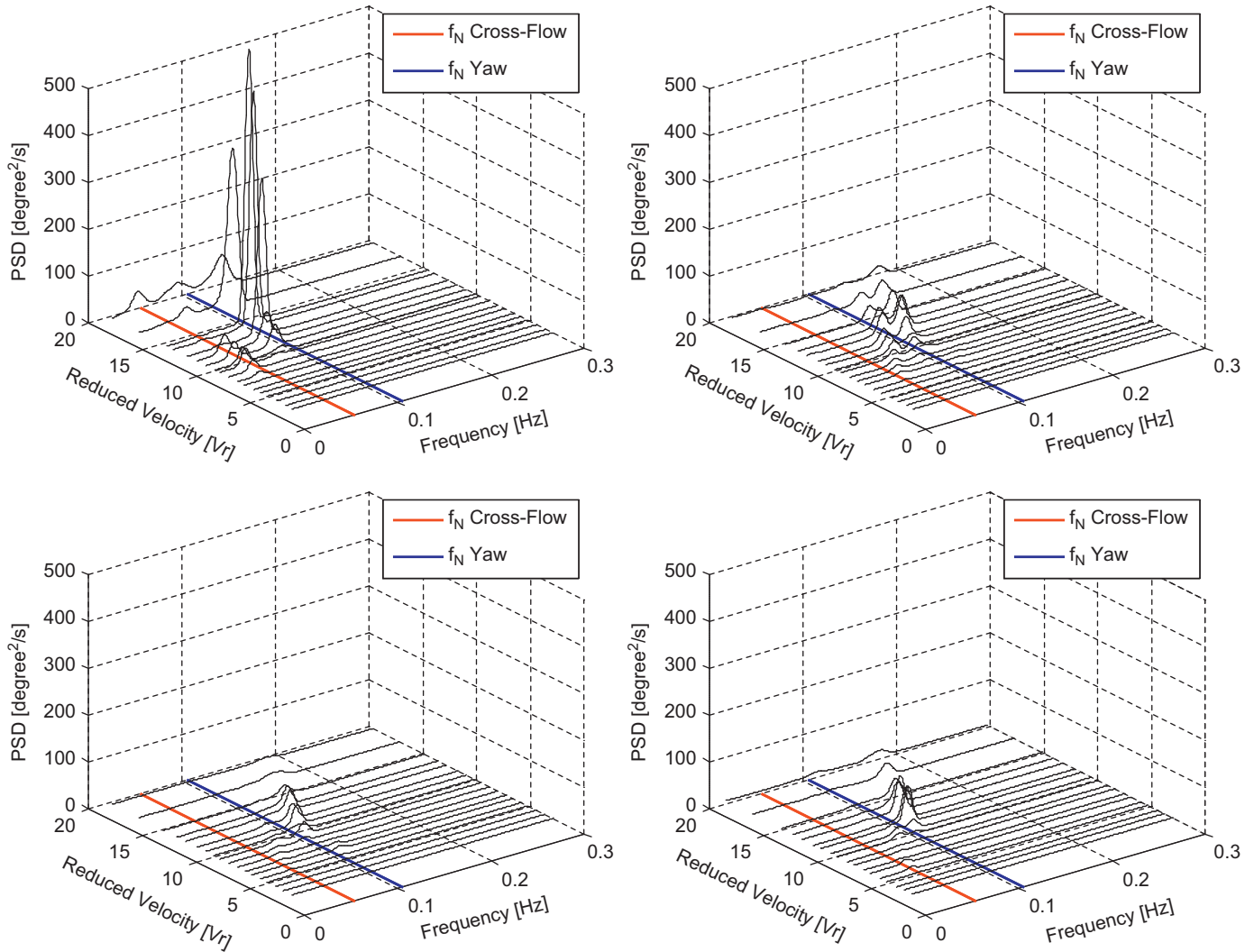
Fig. 29. Power spectrum density from FFT of the yaw motion as a function of reduced velocity and frequency for 0°, 15°, 30° and 45° incidences.

changes and the fluid force oscillates. If the oscillating fluid force tends to increase motion, the structure is dynamically unstable and very large-amplitude motion can result. This phenomenon is known as galloping.

Most galloping analyses utilize quasi-steady dynamics; i.e. the fluid force on the structure is assumed to be solely determined by the instantaneous relative velocity, thus the fluid forces can be measured in wind-tunnel tests on stationary models held at various angles. The quasi-steady assumption is valid only if the frequency of the periodic components of fluid force, associated with vortex shedding, is well above the natural frequency of the structure, $f_s \gg f_0$. This requirement is often met at a higher reduced velocities such that $V_r > 20.0$ (see Bearman et al., 1987).

Applying the quasi-steady theory of galloping, as described in Blevins (2001), the critical velocity for the onset of transverse galloping instability is

$$\frac{U_{crit}}{f_0 D} = \frac{4(m+m_a)(2\pi\zeta_y)}{\rho A_0 D} \bigg/ \left(\frac{\partial C_Y}{\partial \alpha}\right)_{\alpha=\emptyset} \tag{14}$$

where $(m+m_a)$ is the total mass of the system including the added mass for the motion in the transverse direction, ζ_y is the damping factor, A_0 is the submerged projected area for 0° incidence, α is the angle of attack, $\partial C_Y/\partial \alpha$ is the slope of the curve of the transverse force coefficient measured experimentally in the stationary model and $\emptyset$ is the heading angle as defined previously.

The critical velocity for the onset of yaw galloping instability is

$$\frac{U_{crit}}{f_6 D} = -\frac{4(J+J_a)(2\pi\zeta_6)}{\rho A_0 L_z D R} \bigg/ \left(\frac{\partial C_{XY}}{\partial \alpha}\right)_{\alpha=\emptyset} \tag{15}$$

where $(J+J_a)$ is the total inertia moment for the yaw motion of the system, ζ_6 is the damping factor for yaw motion, $\partial C_{XY}/\partial \alpha$ is the slope of the curve of the yaw moment coefficient measured experimentally in the stationary model, L_z is the vertical moment arm considered and R is the half length of the platform.

Considering our case, the in-line force coefficient (C_X), transverse force coefficient (C_Y) and yaw moment (C_{XY}) obtained experimentally for the stationary semi-submersible model is presented in Fig. 33.

Blevins and Iwan (1974) studied the galloping phenomenon for the two degrees-of-freedom system. According to the authors, if the system motions in the transverse direction and the yaw motion can be considered uncoupled or the natural frequencies of these motions are distant, it is possible to apply Eqs. (14) and (15) separately. Using this assumption, the critical reduced velocity for the motions in the transverse direction and for yaw motions were calculated for 0°, 15°, 30° and 45° incidences for the semi-submersible platform model and presented in Table 5. The values of slope $\partial C_Y/\partial \alpha$ and $\partial C_{XY}/\partial \alpha$ are calculated for each incidence using the 3rd degree polynomial fit of the experimental data up to 50°, as presented in Figs. 34 and 35.
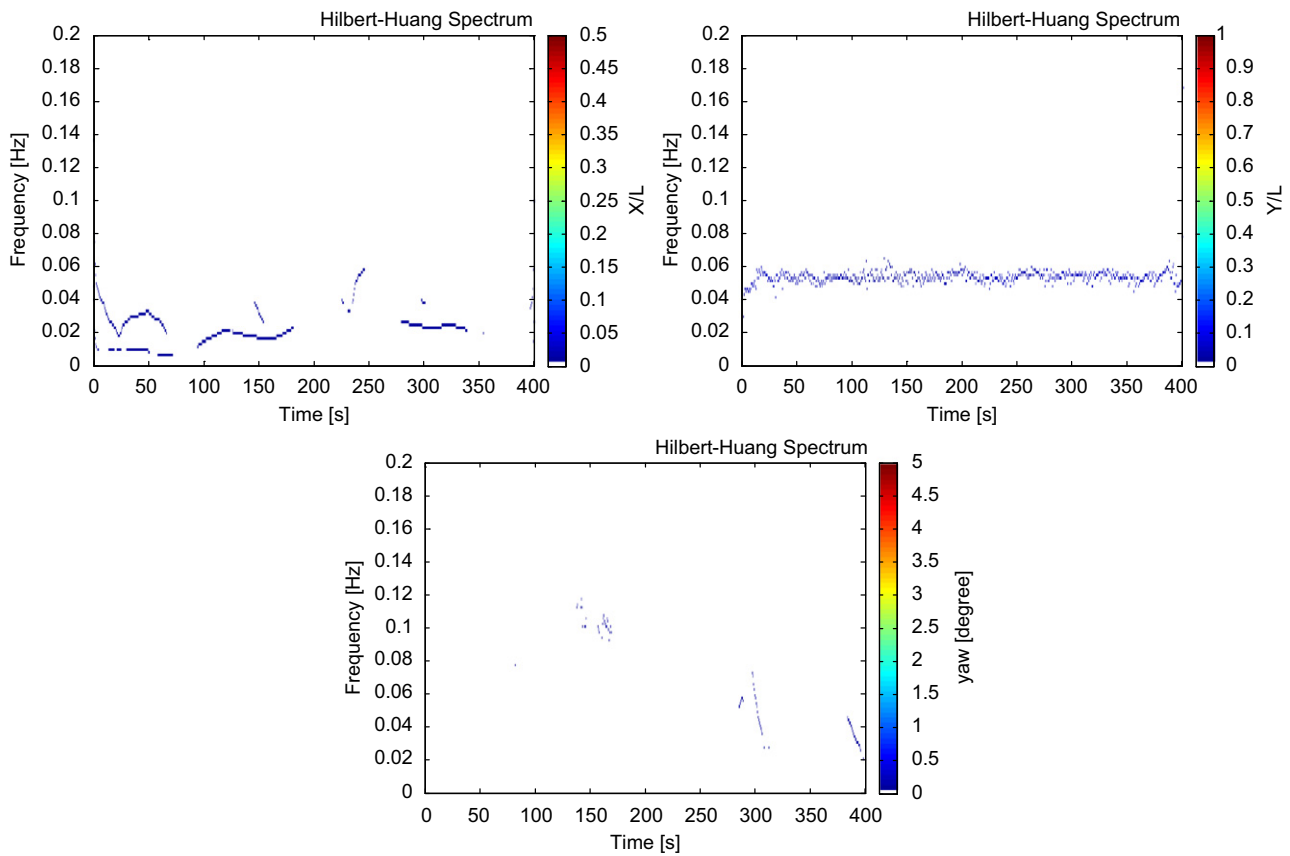
Fig. 30. Example of the Hilbert Spectrum for V_r=3.68 and 45° incidence for different motions: (a) in-line; (b) transverse; and (c) yaw.
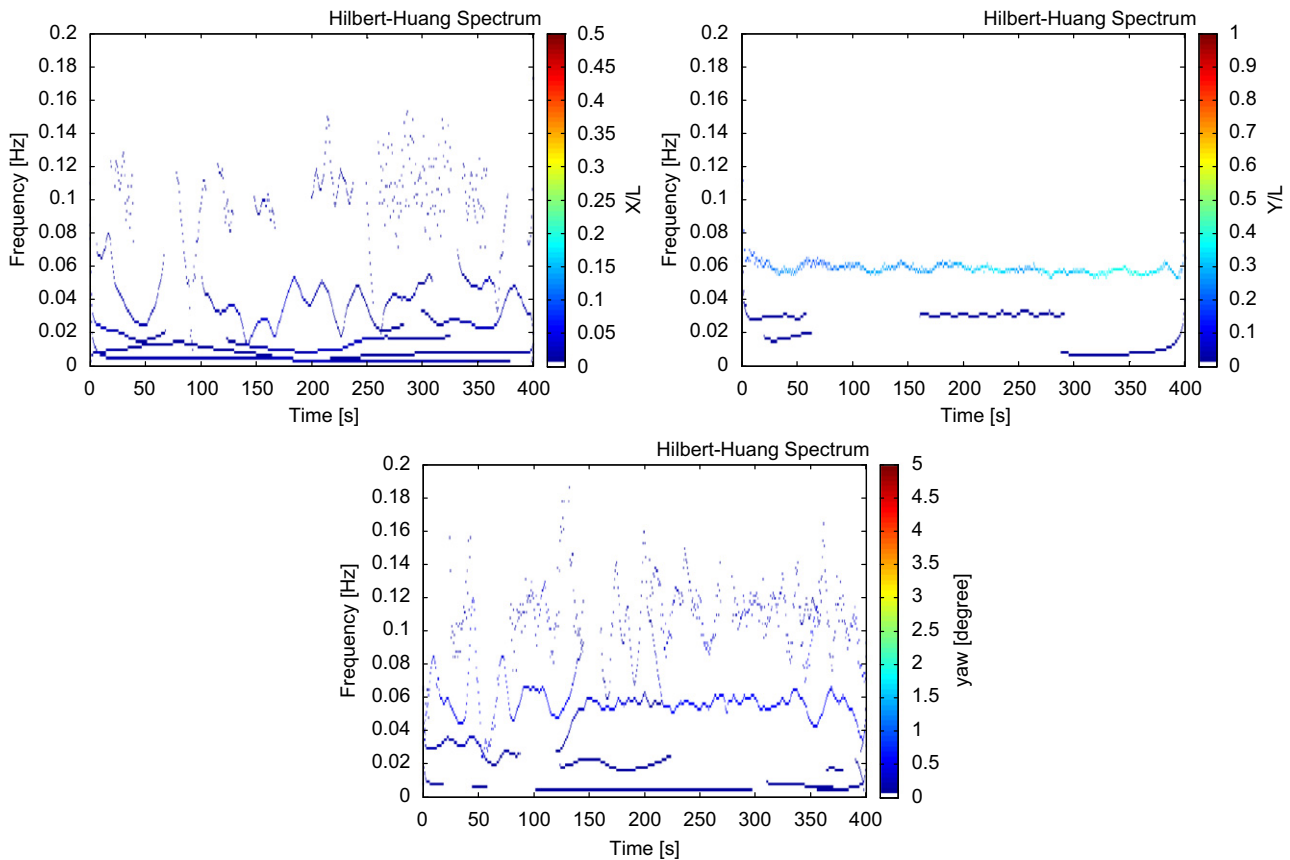
Fig. 31. Example of the Hilbert Spectrum for V_r=6.68 and 45° incidence for different motions: (a) in-line; (b) transverse; and (c) yaw.
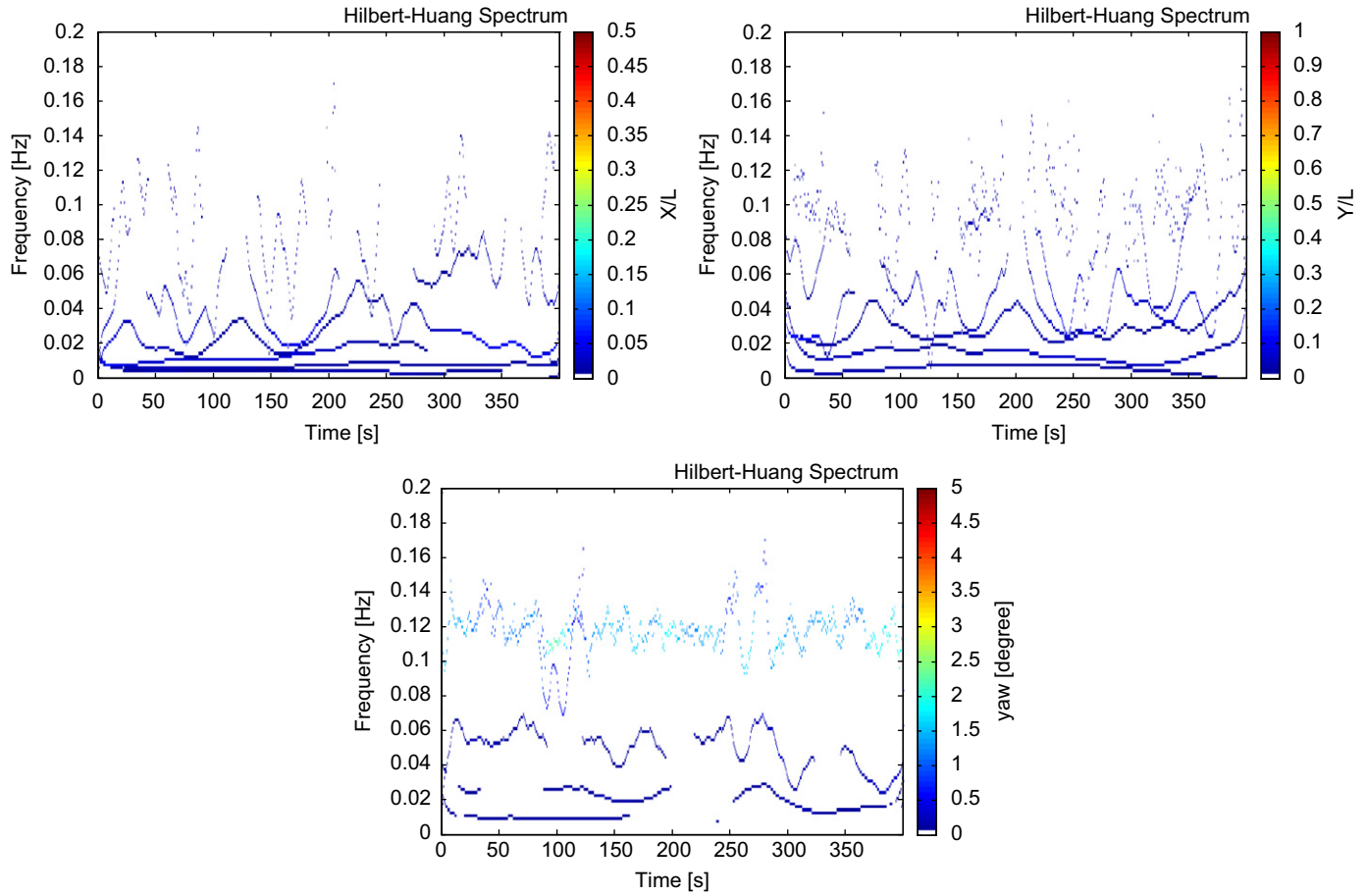
Fig. 32. Example of the Hilbert Spectrum for $V_r=11.78$ and 45° incidence for different motions: (a) in-line; (b) transverse; and (c) yaw.
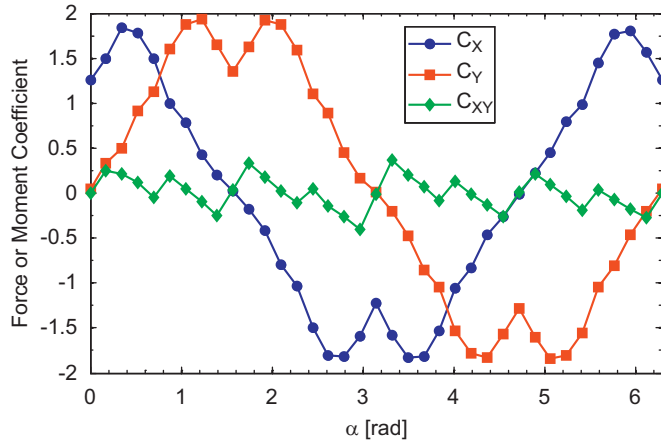

Fig. 33. In-line, transverse and yaw force coefficients for a stationary model of the semi-submersible.

Table 5
Critical reduced velocity of transverse and yaw galloping.

Incidence angle, ∅	$\sigma C_Y/\sigma\alpha$	Critical reduced velocity for transverse direction, $V_{r\ crit}$	$\sigma C_{XY}/\sigma\alpha$	Critical reduced velocity for yaw motion, $V_{r6\ crit}$
0°	1.64	3.91	2.76	Stable
15°	1.43	3.55	−0.26	7.68
30°	1.70	2.52	−0.84	2.02
45°	2.43	1.54	1.02	Stable

It is possible to verify that the values of critical reduced velocity for galloping is lower than 8.0 for all cases, except for the stable ones in 0° and 45° in yaw; nevertheless, in the range of reduced velocities $1.0 < V_r < 20.0$ the quasi-steady assumption is questionable and vortex-induced vibrations may occur (see Olivari, 1983; Bearman et al., 1987).

Examples by Parkinson and Wawzonek (1981), Modi and Slater (1983) and Bearman et al. (1987) showed the existence of vortex resonance effects for low reduced velocity, $V_r < 20.0$ and galloping-like instabilities for the same system for $V_r > 20.0$. The coexistence of these two behaviors may occur for semi-submersible platforms for different reduced velocity ranges, yet it is not possible to conclude the same by means of the present tests, for which the highest reduced velocity is 20.0.

6. Conclusions

This paper discusses the VIM small-scale model tests carried out on a semi-submersible with four square columns at the Institute of Technological Research (IPT), São Paulo, Brazil. The tests aimed at investigating the effects of current incidence angle and hull appendages. Eight different incidence angles were tested in a reduced velocity range from 2.5 up to 20.0, which corresponds to a Reynolds number range from 6000 up to 85,000. The main results comprise motions in the transverse and in-line direction, as well as yaw motions. The following conclusions were drawn.

The largest VIM in the transverse direction was observed for 30°, 45°, 210° and 225°. In general, the VIM in the transverse
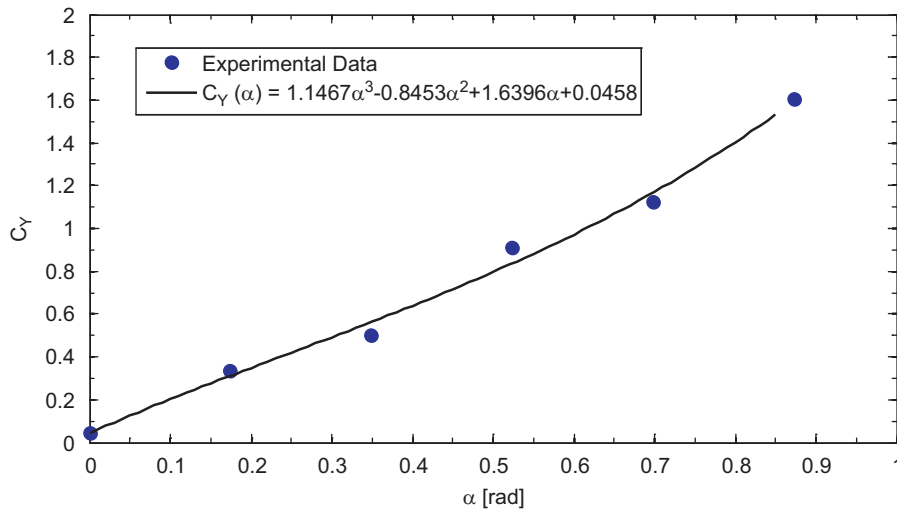
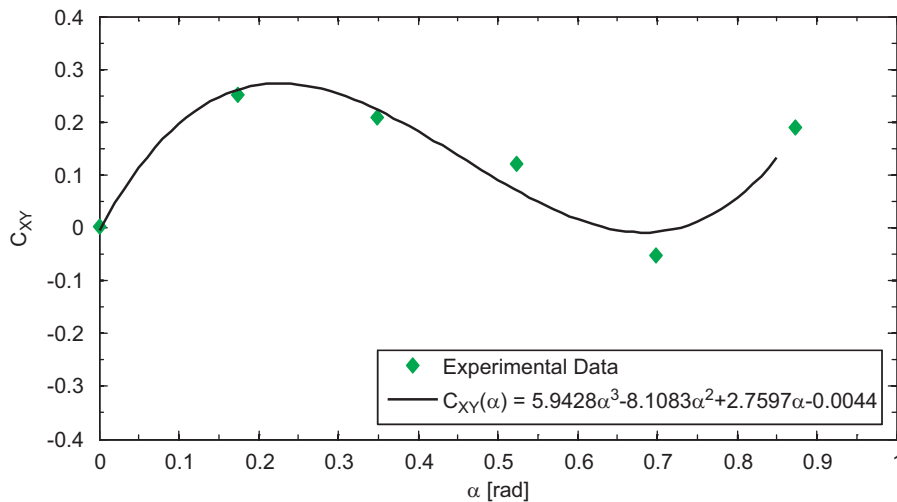**Fig. 34.** Experimental data of transverse force coefficient for the semi-submersible platform model.

Fig. 35. Experimental data of yaw moment coefficient for the semi-submersible platform model.

direction occurs in a range of $4.0 \leq V_r \leq 14.0$ with peaks around $7.0 \leq V_r \leq 8.0$. The largest amplitudes obtained were $A_y/L \cong 0.4$, where L is the width of the column. The experimental results showed that the hard pipes located at columns were the hull appendages with greatest influence in the VIM response of the semi-submersible. The 0° and 180° incidences showed the largest difference between themselves.

The motions in the in-line direction were presented in the range of $4.0 \leq V_r \leq 10.0$ for all incidence conditions, but with small amplitudes $A_x/L < 0.15$ and peak in $V_r \cong 6.0$. Although the largest amplitudes in the transversal and in-line direction occur at the same time, the motions in the XY plane did not present an eight-shaped trajectory. In the transverse synchronization range, the VIM occurs along the semi-submersible diagonals, except for the 0° incidence.

Considerable yaw motion oscillations were verified in these tests. A synchronization region could be identified for yaw motions for reduced velocities up to 15.0, considering the yaw natural period in still water. The largest yaw motions were verified for the 0° and 180° incidences and the maxima amplitudes around $A \cong 4.5°$.

Synchronization range for transverse and yaw motions suggested a resonance behavior indicating the vortex-induced

motions for reduced velocities up to 20.0. A galloping behavior, or a mixed VIV-galloping behavior, may occur for a reduced velocity higher than 20.0, but this range of velocities was not performed in the present work.

The aspects studied here, namely the effects of current incidence angle and hull appendages showed to be decisive in the VIM behavior, and need to be considered in the design phase, not only for risers and mooring lines definition, but for the hull design. Part II of this work will present results showing the influence of external damping, different draft conditions and mainly simultaneous wave and current incidence.

Acknowledgments

References

Bearman, P.W., Gartshore, I.S., Maull, D.J., Parkinson, G.V., 1987. Experiments on flow-induced vibration of a square-section cylinder. J. Fluids Struct. 1, 19–34.

Blevins, R.D., 2001. Flow-induced Vibration, second edition Krieger Publishing Company, Malabar, FL, pp. 104–152.

Blevins, R.D., Iwan, W.D., 1974. The galloping response of two-degree-of-freedom system. J. Appl. Mech. 41, 1113–1118.

Cheng, J., Cao, P., Xiang, S., 2011. Wet tree semi-submersible with SCRs for 4000 ft water depth in the Gulf of Mexico. In: Proceedings of the 29th International Conference on Ocean, Offshore and Arctic Engineering, Rotterdam, The Netherlands, OMAE2011-50002.

Cueva, M., Fujarra, A.L.C., Nishimoto, K., Quadrante, L., Costa A., 2006. Vortex induced motion: model testing of a monocolumn floater. In: Proceedings of the 25th International Conference on Offshore Mechanics and Arctic Engineering, Hamburg, Germany, OMAE2006-92167.

Dutta, S., Muralidhar, K., Panigrahi, P.K., 2003. Influence of the orientation of a square cylinder on the wake properties. Exp. Fluids 34, 16–23.

Dutta, S., Panigrahi, P.K., Muralidhar, K., 2008. Experimental investigation of flow past a square cylinder at an angle incidence. ASCE J. Eng. Mech. 134 (9), 788–803.

Finn, L.D., Maher, J.V., Gupta, H., 2003. The cell spar and vortex induced vibrations. In: Proceedings of the Offshore Technology Conference (OTC 2003), Houston, USA, OTC2003-15244.

Fujarra, A.L.C., Rosetti, G.F., de Wild, J., Gonçalves, R.T., 2012. State-of-art on vortex-induced motion: a comprehensive survey after more than one decade of experimental investigation. In: Proceedings of the 31st International Conference on Ocean, Offshore and Arctic Engineering, Rio de Janeiro, Brazil, OMAE2012-83561.

Gonçalves, R.T., Fujarra, A.L.C., Rosetti, G.F., Nishimoto, K., 2010. Mitigation of vortex-induced motion (VIM) on a monocolumn platform: forces and movements. J. Offshore Mech. Arct. Eng. 132 (4), 041102.

Gonçalves, R.T., Franzini, G.R., Rosetti, G.F., Fujarra, A.L.C., Nishimoto, K., 2012a. Analysis methodology for vortex-induced motions (VIM) of a monocolumn platform applying the Hilbert–Huang transform method. J. Offshore Mech. Arct. Eng. 134 (1), 011103.

Gonçalves, R.T., Rosetti, G.F., Fujarra, A.L.C., Nishimoto, K., 2012b. An overview of relevant aspects on VIM of spar and monocolumn platforms. J. Offshore Mech. Arct. Eng. 134 (1), 014501.

Gonçalves, R.T., Rosetti, G.F., Fujarra, A.L.C., Nishimoto, K., 2012c. Experimental comparative study on vortex-induced Motion (VIM) of a monocolumn platform. J. Offshore Mech. Arct. Eng. 134 (1), 011301.

Hong, Y., Choi, Y., Lee, J., Kim, Y., 2008. Vortex-induced motion of a deep-draft semi-submersible in current and waves. In: Proceeding of the 18th International Offshore and Polar Engineering Conference, Vancouver, BC, Canada.

Huang, N.E., Shen, Z., Long, S.R., Wu, M.C., Shih, H.H., Zheng, Q., Yen, N.-C., Tung, C.C., Liu, H.H., 1998. The empirical mode decomposition and the Hilbert spectrum for nonlinear and non-stationary time series analysis. Proc. R. Soc. London A, 903–995.

Huang, K., Chen, X., Kwan, C.-T., 2003. The impact of vortex-induced motions on mooring system design for spar-based installations. In: Proceedings of the Offshore Technology Conference. OTC 2003, Houston, USA, OTC2003-15245.

Hussain, A., Nah, E., Fu, R., Gupta, A., 2009. Motion comparison between a conventional deep draft semi-submersible and a dry tree semi-submersible. In: Proceeding of the 28th International Conference on Ocean, Offshore and Arctic Engineering, Hawaii, USA, OMAE2009-80006.

Irani, M., Finn, L., 2005. Improved strake design for vortex induced motions of spar platforms. In: Proceedings of the 24th International Conference on Offshore Mechanics and Arctic Engineering, Halkidiki, Greece, OMAE2005-67384.

Kim, J.-W., Magee, A., Guan, K.Y.H., 2011. CFD simulation of flow-induced motions of a multi-column floating platform. In: Proceedings of the 29th International Conference on Ocean, Offshore and Arctic Engineering, Rotterdam, The Netherlands, OMAE2011-49437.

Lam, K., Lo, S.C., 1992. A visualization study of cross-flow around four cylinders in a square configuration. J. Fluids Struct. 6, 109–131.

Lam, K., Fang, X., 1995. The effect of interference of four equispaced cylinders in cross flow on pressure and force coefficients. J. Fluids Struct. 9, 195–214.

Lam, K., Li, J.Y., Chan, K.T., So, R.M.C., 2003a. Flow pattern and velocity field distribution of cross-flow around four cylinders in a square configuration at a low Reynolds number. J. Fluids Struct. 17, 665–679.

Lam, K., Li, J.Y., So, R.M.C., 2003b. Force coefficients and Strouhal numbers of four cylinders in cross flow. J. Fluids Struct. 18, 305–324.

Magee, A., Sheikh, R., Guan, K.Y.H., Choo, J.T.H., Malik, A.M.A., Ghani, M.P.A., Abyn, H., 2011. Model tests for VIM of multi-column floating platforms. In: Proceedings of the 29th International Conference on Ocean Offshore and Arctic Engineering, Rotterdam, The Netherlands, OMAE2011-49151.

Mercier, R.S., Ward, E.G., 2003. Spar vortex-induced motions. In: Proceedings of the MMS/OTRC Workshop, Navasota, TX, USA.

Modi, V.J., Slater, J.E., 1983. Unsteady aerodynamics and vortex induced aeroelastic instability of a structural angle section. J. Wind Eng. Ind. Aerodyn. 11, 321–334.

Noce, R., Husem, I., 2011. The first dry tree semisubmersible drilling and production platform sold. In: Proceedings of the Offshore Technology Conference Brasil. Rio de Janeiro, Brazil, OTC-22505.

Norberg, C., 1993. Flow around rectangular cylinders: pressure forces and wake frequencies. J. Wind Eng. Ind. Aerodyn. 49, 187–196.

Olivari, D., 1983. An investigation of vortex shedding and galloping induced oscillation on prismatic bodies. J. Wind Eng. Ind. Aerodyn. 11, 307–319.

Oakley Jr., O.H., Constantinides, Y., 2007. CFD truss spar hull benchmarking study. In: Proceedings of the 26th International Conference on Offshore Mechanics and Arctic Engineering, San Diego, CA, USA, OMAE2007-29150.

Parkinson, G.V., Wawzonek, M.A., 1981. Some considerations of combined effects of galloping and vortex resonance. J. Wind Eng. Ind. Aerodyn. 8, 135–143.

Rijken, O., Leverette, S., Davies, K., 2004. Vortex induced motions of semi submersible with four square columns. In: Proceedings of the 16th Deep Offshore Technology Conference and Exhibition, New Orleans, LA, USA.

Rijken, O., Leverette, S., 2008. Experimental study into vortex induced motion response of semi submersible with square columns. In: Proceedings of the 27th International Conference on Offshore Mechanics and Arctic Engineering, Estoril, Portugal, OMAE2008-57396.

Rijken, O., Leverette, S., 2009. Field measurements of vortex induced motions of a deep draft semisubmersible. In: Proceedings of the 28th International Conference on Ocean, Offshore and Arctic Engineering, Honolulu, HI, USA, OMAE2009-79803.

Rijken, O., Schuurmans, S., Leverette, S., 2011. Experimental investigation into the influences of SCRs and appurtenances on deepdraft semisubmersible vortex induced motion response. In: Proceedings of the 30th International Conference on Ocean, Offshore and Arctic Engineering, Rotterdam, The Netherlands, OMAE2011-49365.

Roddier, D., Finnigan, T., Liapis, S., 2009. Influence of the Reynolds number on spar Vortex Induced Motions (VIM): multiple scale model test comparisons. In: Proceedings of the 28th International Conference on Ocean, Offshore and Arctic Engineering, Honolulu, HI, USA, OMAE2009-79991.

Sagrilo, L.V.S., Siqueira, M.Q., Lacerda, T.A.G., Ellwanger, G.B., Lima, E.C.P., Siqueira, E.F.N., 2009. VIM and wave-frequency fatigue damage analysis for SCRs connected to monocolumn platforms. In: Proceedings of the 28th International Conference on Ocean, Offshore and Arctic Engineering, Honolulu, HI, USA, OMAE2009-79431.

Sarpkaya, T., 2004. A critical review of intrinsic nature of vortex-induced vibrations. J. Fluids Struct. 19, 389–447.

Sayers, A.T., 1988. Flow interference between four equispaced cylinders when subject to a cross flow. J. Wind Eng. Ind. Aerodyn. 31, 9–28.

Sayers, A.T., 1990. Vortex shedding from groups of three and four equispaced cylinders situated in a cross flow. J. Wind Eng. Ind. Aerodyn. 34, 213–221.

Stansberg, C.T., 2008. Current effects on a moored floating platform in a sea state. In: Proceedings of the 27th International Conference on Offshore Mechanics and Arctic Engineering, Estoril, Portugal, OMAE2008-57621.

Tahar, A., Finn, L., 2011. Vortex induced motion (VIM) performance of the multi column floater (MCF)—drilling and production unit. In: Proceedings of the 29th International Conference on Ocean, Offshore and Arctic Engineering, Rotterdam, The Netherlands, OMAE2011-50347.

van Dijk, R.R., Magee, A., Perryman, S., Gebara, J., 2003. Model test experience on vortex induced vibrations of truss spars. In: Proceedings of the Offshore Technology Conference (OTC 2003), Houston, USA, OTC2003-15242.

Waals, O.J., Phadke, A.C., Bultema, S., 2007. Flow induced motions of multi column floaters. In: Proceedings of the 26th International Conference on Offshore Mechanics and Arctic Engineering, San Diego, CA, USA, OMAE2007-29539.

Wang, Y., Yang, J., Peng, T., Li, X., 2009. Model test study on vortex-induced motions of a floating cylinder. In: Proceedings of the 28th International Conference on Ocean, Offshore and Arctic Engineering, Honolulu, HI, USA, OMAE2009-79134.

Wang, Y., Yang, J., Peng, T., Lu, H., 2010. Strake design and VIM-suppression study of a cell-truss spar. In: Proceedings of the 29th International Conference on Ocean, Offshore and Arctic Engineering, Shanghai, China, OMAE2010-20225.

Xiang, S., Cao, P., Rijken, O., Ma, J., Chen, Y., 2010. Riser VIM fatigue design induced by deep draft semi-submersible. In: Proceedings of the 29th International Conference on Ocean, Offshore and Arctic Engineering, Shanghai, China, OMAE2010-20339.

Xu, Q., 2011. A new semisubmersible design for improved heave motion, vortex-induced motion and quayside stability. In: Proceedings of the 29th International Conference on Ocean, Offshore and Arctic Engineering, Rotterdam, The Netherlands, OMAE2011-49118.

Yen, S.C., Yang, C.W., 2011. Flow patterns and vortex shedding behavior behind a square cylinder. J. Wind Eng. Ind. Aerodyn. 99, 868–878.

Zdravkovich, M.M., 1987. The effects of interference between circular cylinders in cross flow. J. Fluids Struct. 1, 239–261.